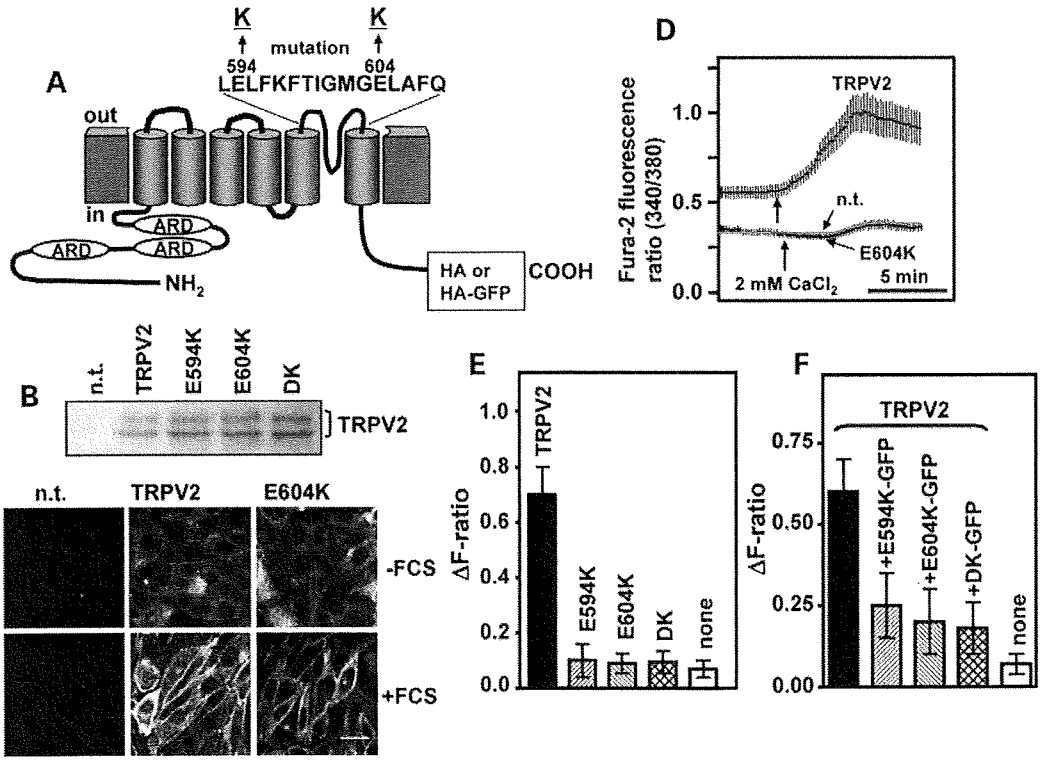

Figure 1. Dominant-negative mutants of TRPV2. (**A**) A schematic drawing of TRPV2 constructions. The C-terminus of TRPV2 was tagged with either the HA-epitope alone or with GFP inserted after the HA-tag. Conserved residues in the putative pore region (Glu594 and Glu604) were substituted with lysine, either individually or together. ARD, ankyrin repeat domain. (**B**) Equal amounts (10 μg) of lysate from CHO cells stably expressing wild-type or mutant TRPV2 were subjected to immunoblot analysis using anti-TRPV2 antibody. (**C**) Immunohistochemical analysis. Cells expressing wild-type TRPV2 or E604K-HA were serum-depleted overnight (−FCS, upper panel); stimulated for 15 min with 10% serum (+FCS, lower panel) and fixed, permeabilized and immunostained with anti-TRPV2 antibody. n.t., no transfection. Scale bar: 50 μm. (**D**) Typical traces from the ratiometric scanning of fura-2 fluorescence. Transfected or non-transfected (n.t., *grey*) cells were placed on glass coverslips and perfused with solution containing 0.5 mM $CaCl_2$. Perfusion with high concentrations of $CaCl_2$ (2 mM) resulted in a rapid increase in the fluorescence ratio in TRPV2-transfectants, but not E604K-HA. (**E**) Summary of fura-2 fluorescence data. The ΔF ratio was calculated by subtracting the resting level of the fluorescence ratio from the maximal level after high Ca^{2+} addition. (**F**) The GFP-tagged TRPV2 constructs were transiently expressed in TRPV2 stable transfectants and the fluorescence data from GFP-positive cells were summarized. Values are means ± SD of more than 20 cells (E and F).

mice, but not much in fibers from *mdx*/Tg mice. Bleb formation in *mdx* fibers was inhibited by more than 60% upon expression of E604K-HA (data not shown). A sustained increase in $[Ca^{2+}]_i$ via surface TRPV2 would result in various phenotypic changes in the skeletal muscles of *mdx* mice via activation of Ca^{2+}-dependent enzymes. Consistent with this idea, the phosphorylation of Ca^{2+}/calmodulin-dependent protein kinase (CaMK)II was significantly higher in *mdx* skeletal muscle compared to controls (Fig. 2A). In contrast, phosphorylated CaMKII was markedly reduced in the *mdx*/Tg mice (Fig. 2A), suggesting a reduced $[Ca^{2+}]_i$ in muscle fibers from these mice.

Transgenic expression of dominant-negative TRPV2 ameliorates muscular dystrophy in *mdx* mice

To determine whether dominant-negative inhibition of TRPV2 could prevent muscular dystrophy, we first analyzed the overall symptoms for muscle degeneration. Expression of E604K-HA in *mdx* mice (*mdx*/Tg) markedly (40–60%) reduced the level of serum creatine kinase (CK), a marker for muscle damage (Fig. 4A), and improved muscle performance as evaluated by a grip test (50–70% of wild-type) (Fig. 4B). The improvement of muscle damage was observed in *mdx*/Tg mice produced from two Tg lines (I and II).

We next analyzed the histological characteristics of skeletal muscles. Skeletal muscle-specific expression of E604K-HA produced no striking morphological changes in the muscles of Tg mice (Fig. 5Ab), and muscle fibers from *mdx*/Tg mice (Fig. 5Ad and f) presented with a healthier appearance compared to their *mdx* counterparts (Fig. 5Ac and e). Among several abnormal morphological indices, dystrophic muscle fibers are known to display a greater variation in their cross-sectional area (23). Muscles from *mdx*/Tg mice exhibited a greater homogeneity compared to *mdx* mice in respect to fiber size variability, determined by averaging the standard deviation of the cross-sectional areas (Fig. 5B). Furthermore, the expression of E604K-HA reduced (60% reduction) the number of fibers with central nuclei (Fig. 5C) in 10 week *mdx*/Tg mice, the area of inflammatory infiltrate (more than 90% reduction) and Evans blue dye (EBD) uptake (marker of membrane integrity, 80% reduction) (Fig. 5D) in similar-aged

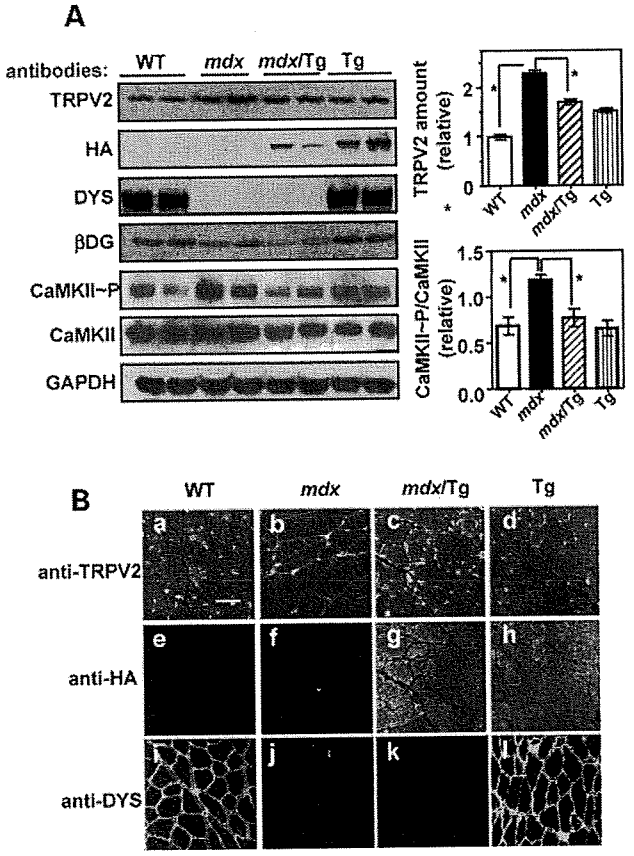

Figure 2. Protein expression pattern in wild-type, *mdx*, Tg and *mdx*/Tg mice. (**A**) Immunoblot analysis with indicated antibodies. The relative amount of TRPV2 was normalized to GAPDH, and phosphorylated CaMKII (CaMKII-P) was normalized to the total amount of CaMKII (right panels). (**B**) Immunohistochemical analysis of TRPV2 and dystrophin in frozen cross sections of skeletal muscle. Double immunostaining was performed using FITC-conjugated rat anti-HA (e–h) and rabbit anti-TRPV2 (a–d) followed by rhodamine-conjugated secondary antibodies. Immunostaining was also performed with anti-dystrophin (i–l) antibody. Surface localization of TRPV2 in *mdx* mice was reduced by crossing with Tg mice (*mdx*/Tg). See Supplementary Material, Fig. S4 for a semi-quantitative analysis. Scale bar: 50 μm.

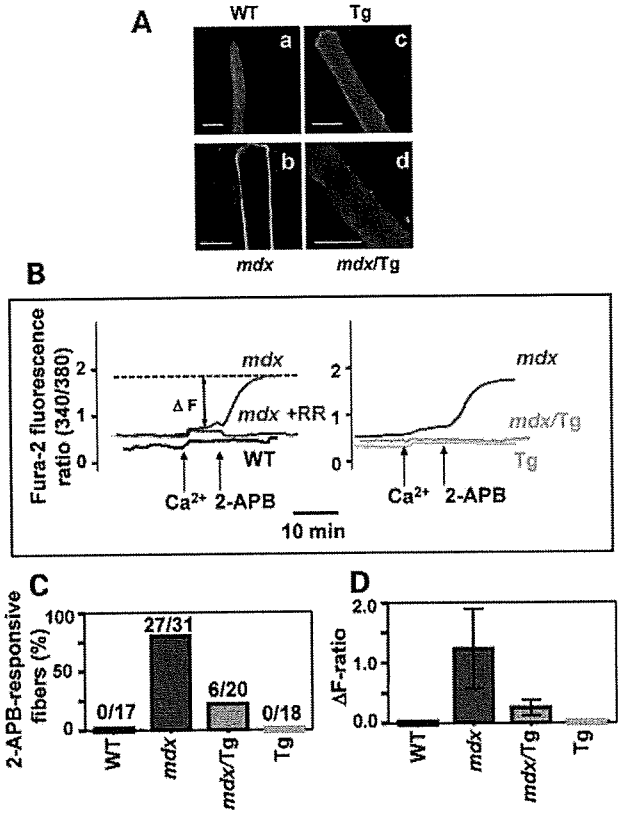

Figure 3. Dominant-negative TRPV2 inhibits a Ca^{2+} abnormality in *mdx* mice. (**A**) FDB muscle fibers isolated from wild-type (a), *mdx* (b), Tg (c) and *mdx*/Tg (d) mice were visualized by immunofluorescence staining with anti-TRPV2 antibody (a–d). Scale, 100 μm. (**B**) Representative traces for the 2-APB-induced increase in the fura-2 fluorescence ratio. Fibers placed in a solution containing 2 mM $CaCl_2$ were stimulated with high Ca^{2+} (5 mM, indicated by arrow) and then 500 μM 2-APB. Ruthenium red was included just in the 2-APB solution (blue line). The Ca^{2+} increase induced by 2-APB was reduced in *mdx*/Tg fibers and completely blocked by ruthenium red (40 μM). (**C**) The ΔF ratio was calculated by subtracting the resting fluorescence ratio from the maximal ratio after inclusion of 2-APB. Fibers exhibiting a ΔF-ratio >0.3 were defined as 2-APB-responsive fibers and plotted. The values for 2-APB-responsive fibers per total number of analyzed fibers from each of 3–4 mice are shown. (**D**) The ΔF-ratio was averaged and plotted (means ± SD).

mice, suggesting that the degeneration of myofibers markedly decreased and subsequent muscle regeneration was reduced in the *mdx*/Tg mice. In addition, Masson's trichrome staining revealed that the foci of fibrosis, reflecting the progressive replacement of myofibers with connective tissue, was frequently detected in *mdx* mice, but the expression of E604K-HA reduced fibrosis more than 60% (Fig. 5E and F). The high level of apoptosis seen in *mdx* muscle was also reduced in *mdx*/Tg muscle (Fig. 5G and H). We observed that the expression of E604K-HA may be somewhat mosaic in *mdx*/Tg muscle as well as Tg muscle as seen in Fig.2Bg and h, thus exerts a different dominant-negative effect on individual muscle fibers. In order to directly check the involvement of this E604K-HA expression, we compared the area stained with incorporated EBD, a marker of cell injury, to the area immunostained with anti-HA or anti-TRPV2 using serial sections (Supplementary Material, Fig. S6). Fibers stained with EBD, which were sometimes observed in *mdx*/Tg mice, corresponded to those showing relatively low expression level of E604K-HA, but the condensed expression of endogenous TRPV2 (Supplementary Material, Fig. S6C). Thus, high membrane expression of endogenous TRPV2 well correlates with pronounced EBD uptake. Taken together, these data suggest that the inhibition of TRPV2 significantly improves muscular dystrophy in *mdx* mice, and TRPV2 may play a pivotal role in causing dystrophic muscle damage.

Adenoviral expression of dominant-negative TRPV2 ameliorates muscular dystrophy in BIO14.6 hamsters

We next examined whether the inhibition of TRPV2 also reduces muscle damage in BIO14.6 hamster, another model of dystrophy. Infection of cultured BIO14.6 myotubes with

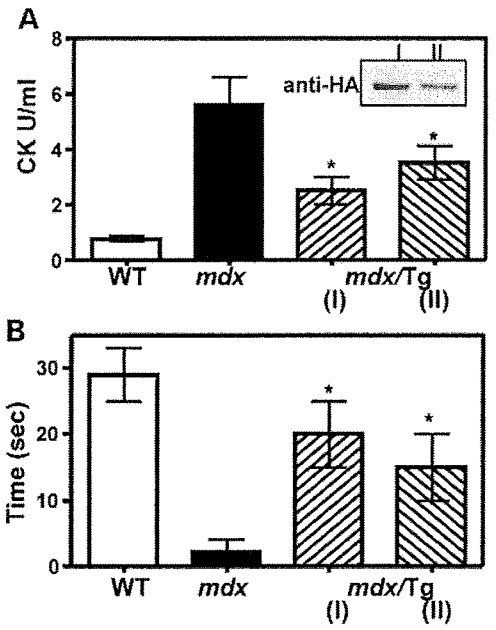

Figure 4. Dominant-negative TRPV2 ameliorates muscle dysfunction in *mdx* mice. (**A**) Serum creatine kinase (CK) levels were compared among 5–10 week old wild-type, *mdx* and *mdx*/Tg mice produced from Tg lines I and II, respectively. Data are means ± SD of 6–21 mice. Protein expression levels of E604K-HA in *mdx*/Tg mice from two Tg lines examined by immunoblot analysis with anti-HA antibody (A inset). (**B**) Muscle function evaluated by grip test in 5–10 week old wild-type, *mdx* and *mdx*/Tg mice produced from Tg lines I and II, respectively. Data are means ± SD of 6–21 mice.

adenovirus carrying DK-HA resulted in the expression of HA-tagged TRPV2 mutant (Fig. 6A). While endogenous TRPV2 was almost exclusively localized in sarcolemma of BIO14.6 myotubes (Fig. 6A and B), upon expression of DK-HA it was translocated from the surface to the intracellular membranes of myotubes, where endogenous and exogenous TRPV2 proteins appeared to be co-localized (Fig. 6Ac). We found that the Ca^{2+}-induced increase in the $[Ca^{2+}]_i$ was markedly suppressed in myotubes infected with adenovirus carrying DK-HA (Fig. 6B). In addition, adenovirally expressed DK-HA reduced the stretch-induced CK release observed in control BIO14.6 myotubes (Fig. 6C), suggesting that the inhibition of TRPV2 is effective for reducing the stretch-induced cell damage to BIO14.6 myotubes. Of note, upon infection of adenovirus, total level of TRPV2 expression does not increase so much, whereas DK-HA is successfully expressed in myotubes (Fig. 6A), suggesting that the exogenous expression of DK-HA may inhibit the expression of endogenous TRPV2. However, the expression of DK-HA clearly changed the distribution pattern of endogenous TRPV2 and suppressed Ca^{2+} abnormality, suggesting that the expression level of DK-HA would be sufficient to affect the function of endogenous TRPV2.

Furthermore, we injected adenovirus carrying β-gal or DK-HA into the quadriceps of 60-day-old BIO14.6 hamsters. Treatment of muscles with adenovirus carrying DK-HA resulted in the expression of HA-tagged TRPV2 mutant (upper panel of Fig. 7A) and reduction in plasma membrane localization of TRPV2 (lower panel of Fig. 7A). Fourteen days later, the muscle degeneration was reduced in DK-HA virus-infected BIO14.6 hamsters compared to those infected with adenoviral β-gal (Fig. 7Ba and b). The number of central nuclei and fiber size variability was reduced (40–50%) upon DK-HA infection (Fig. 7C), and TUNEL staining additionally revealed a marked reduction (~80%) in apoptosis in DK-HA-infected muscles (Fig. 7Bc and d, and C). Together, these data demonstrate that, similar to the *mdx* mouse model, the inhibition of TRPV2 is capable of greatly ameliorating muscular dystrophy in the BIO14.6 hamster model.

DISCUSSION

Abnormal Ca^{2+}-handling is a hallmark of muscle dysfunction in muscular dystrophy. In the present study, we demonstrated that the Tg or adenoviral expression of mutant TRPV2 reduces the $[Ca^{2+}]_i$ increase and muscle degeneration, and ameliorated muscle dystrophy, in the *mdx* mouse and BIO14.6 hamster models *in vivo* and *in vitro*. We presented evidence that the beneficial effect of mutant TRPV2 is due to the dominant-negative inhibition of endogenous TRPV2, resulting in suppressed Ca^{2+}-permeation and reduced plasma membrane expression. In addition to the decreased Ca^{2+} influx in isolated FDB fibers, we observed that the enhanced phosphorylation of CaMKII in *mdx* mice was reduced after crossing them with Tg mice, strongly suggesting that the increase in intracellular Ca^{2+} level was indeed reduced in the skeletal muscle of *mdx*/Tg mice. This inhibition likely occurs from the oligomerization of the mutant subunit with endogenous TRPV2 subunits upon assembly of TRPV2 channels because TRPV2 is thought to function as a homo-oligomer (17,18,24). In fact, this is supported by the finding that the subcellular localization of endogenous TRPV2 is markedly affected by the exogenous expression of mutant TRPV2 in *mdx*/Tg mice. Although a recent study reported that TRPV2 may also be capable of forming hetero-oligomers with TRPV1 and/or TRPV3 (25), the expression of TRPV1 and TRPV3 was not detected by immunoblot analysis in mouse skeletal muscle (Supplementary Material, Fig. S7). On the other hand, the TRPC family has been reported to be involved in abnormal Ca^{2+} handling in the skeletal muscle of *mdx* mice (14). However, we observed that the $[Ca^{2+}]_i$ was increased by 2-APB, a TRPC channel antagonist (26). Furthermore, a significant difference was not observed in the expression of TRPC family members (TRPC1, 3, 4 and 6) among four kinds of mice (Supplementary Material, Fig. S7). Therefore, the involvement of TRPC channels would be minor. Thus, our present data, together with previous data (16), strongly suggest that TRPV2 plays a crucial pathological role in the Ca^{2+}-induced muscle degeneration of dystrophic muscles.

Our findings also provide convincing validation of the therapeutic potential of TRPV2 for muscular dystrophy. This protein has several advantages as a therapeutic target. First, most TRPV2 localizes to the intracellular membranes in normal, healthy skeletal muscle, but it translocates to the surface membrane upon muscle degeneration (16); hence, specific inhibitors against TRPV2 are predicted to only act

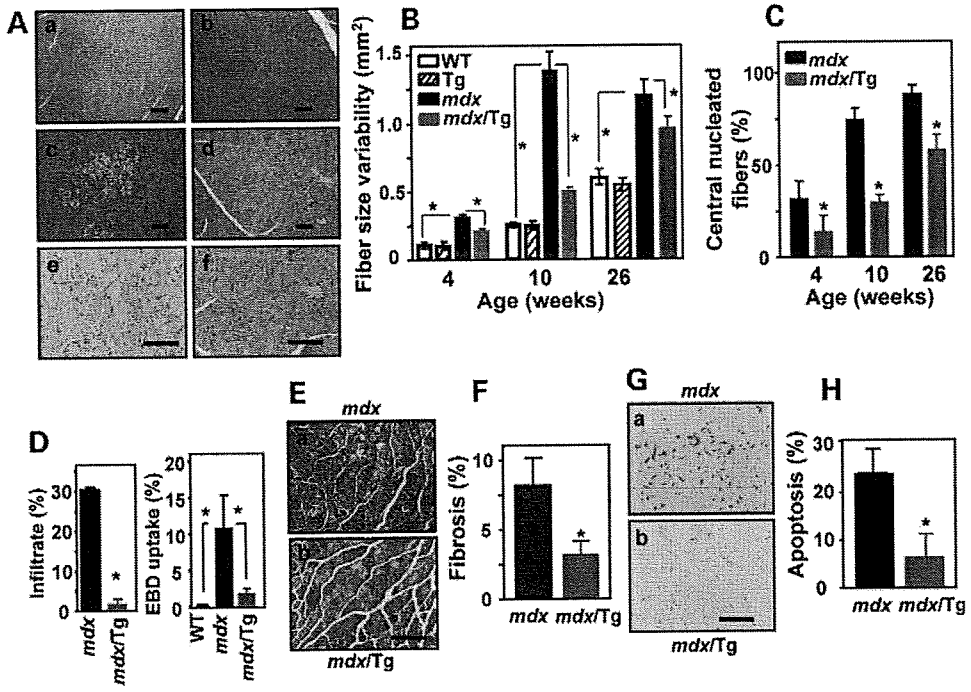

Figure 5. Dominant-negative TRPV2 attenuates muscle degeneration in *mdx* mice. (**A**) Representative images for H&E staining of quadricep sections from wild type (a), Tg (b), *mdx* (c and e) and *mdx*/Tg (d and f) mice. (a–d) Twenty-six weeks old, (e and f) 10 weeks old. Scale, 100 μm. (**B–D**) Histological parameters were measured using H&E stained sections. Sections covering more than 1000 fibers from three to four mice were used for an analysis of each group. Cross-sectional areas of each individual fiber were measured and the variability of muscle fiber size was determined by averaging the standard deviations of data (B). The number of centrally nucleated fibers (C) was also measured using the same histological sections. (D) Percentage of inflammatory infiltration area measured using the histological sections from 7 to 10 week old *mdx* and *mdx*/Tg (line I) mice. Data are means ± SD of four mice. The percentage of EBD-positive area (cf. Supplementary Material, Fig. S6). Data are means ± SD of four mice. (**E** and **F**) Masson's trichrome staining of 26 week old *mdx* (a) and *mdx*/Tg (b) mice, and measurements of the area of fibrosis. (**G** and **H**) TUNEL labeling of sections of gastrocnemius muscle samples from 10 week old *mdx* (a) or *mdx*/Tg (b) mice, and the number of fibers exhibiting apoptosis. For histological analysis, sections covering more than 1000 fibers from three to four mice were used for measurements. Scale bar, 100 μm.

on degenerative muscles. Second, surface translocation and the subsequent activation of TRPV2 may occur in a wide range of genetic or non-genetic muscle diseases (16). For example, we recently observed that the surface translocation of TRPV2 also occurs in the hearts of idiopathic cardiomyopathy patients (unpublished observation). Thus, specific inhibitors against TRPV2 could be potentially useful for the treatment of various degenerative muscle diseases.

In this study, we presented evidence that the inhibition of TRPV2 is able to ameliorate several indices characterizing the dystrophic pathology. However, it is important to consider that the pathology of dystrophin-deficient muscles covers a broader area that includes susceptibility to exercise-induced injury, oxidative stress and an impaired regenerative capacity. We observed that the inhibition of TRPV2 resulted in a different degree of amelioration in dystrophic indices examined in this study, reflecting the complexity of this disease. For example, good amelioration (60–90%) was seen in all dystrophic parameters in young *mdx*/Tg mice (4–10 weeks), but in old mice (more than 26 weeks) only 30–40% amelioration was seen in fiber size variability and in number of centrally nucleated fibers, although fibrosis was markedly reduced even in old mice. In young *mdx*/Tg mice, it is likely that dominant-negative TRPV2 decreases the susceptibility of dystrophic muscles to the on-going cycles of degeneration and regeneration induced by contraction, while in older mice such a cycle may be saturated and no more changed. Thus, the inhibition of TRPV2 appears to primarily promote the retardation of muscle degeneration onset. Furthermore, we observed a partial amelioration (40–60%) of serum CK levels, when compared with apparently better improvement of tissue injury in limbs muscles such as quadriceps examined. This would be due to the fact that serum CK levels reflect the overall state of all muscles including diaphragm and back muscle not examined in this study. Although dominant-negative TRPV2 does not completely prevent dystrophic pathology, our present data suggest that TRPV2 would be a key molecule to link the disruption of DGC with muscle degeneration.

An important issue is the molecular mechanism by which TRPV2 translocates to the plasma membrane and becomes activated in dystrophic muscles. In both *mdx* and *mdx*/Tg mice, it is likely that the muscles are subjected to continuous mechanical stress caused by the dystrophin deficiency. Such mechanical stretch may enhance the secretion of various hormones or bioactive substances, which potentially promote TRPV2 translocation via receptor stimulation because translocation is known to occur in response to various signals,

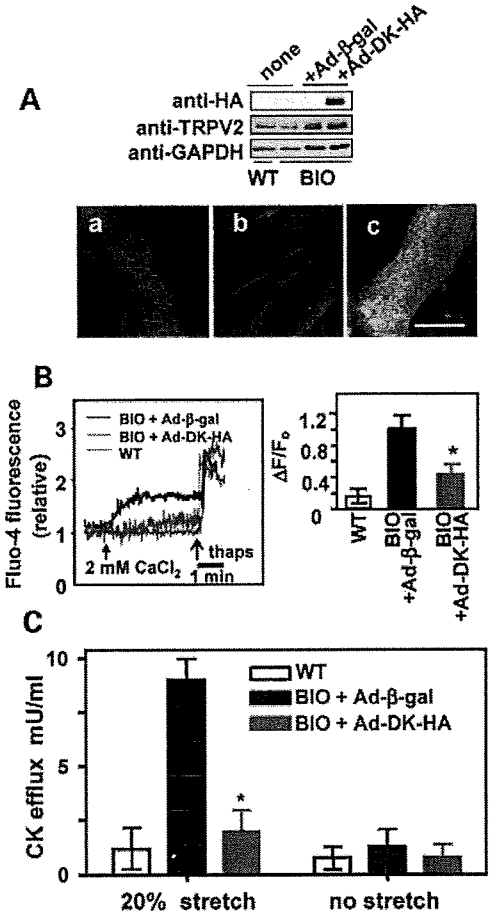

Figure 6. Adenoviral dominant-negative TRPV2 improves abnormal Ca^{2+} handling and muscle degeneration in cultured myotubes from BIO14.6 hamsters. (**A**) Immunoblot analysis of wild-type (lane 1) and BIO14.6 myotubes (lanes 2–4) infected with Ad-β-gal (lane 3) or Ad-DK-HA (lane 4) for expressed mutant TRPV2 (DK-HA), total TRPV2 and GAPDH (anti-GAPDH antibody). Lower panel: immunocytochemistry of TRPV2 in cultured myotubes. Myotubes from wild-type (a) and BIO14.6 infected with Ad-β-gal (b) were immunostained with anti-TRPV2. BIO 14.6 myotubes infected with Ad-DK-HA were double-stained with anti-TRPV2 (red) and anti-HA (green), and then two images were merged. (**B**) Typical trace of the extracellular Ca^{2+}-induced change in fluo-4 fluorescence in wild-type (blue line) or BIO14.6 myotubes infected with Ad-β-gal (black line) or Ad-DK-HA (red line). thaps, thapsigargin. External Ca^{2+}-induced maximal fluorescence increments were normalized by the initial value ($\Delta F/F_0$). (**C**) Wild type or adenovirus-infected BIO14.6 myotubes were subjected to 20% elongation 1 h and the level of CK released to the medium was measured.

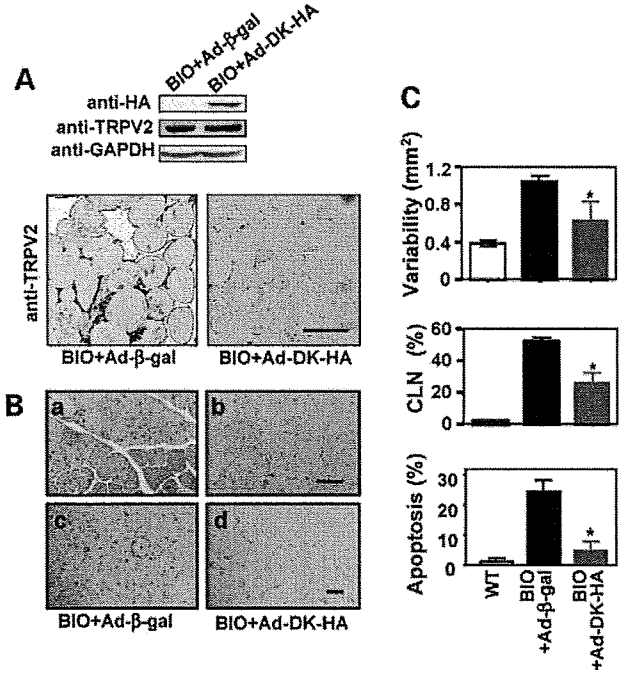

Figure 7. Adenoviral dominant-negative TRPV2 ameliorates muscular dystrophy of skeletal muscle from BIO14.6 hamsters. (**A**) Immunoblot analysis of BIO14.6 hamster skeletal muscles which were intramuscularly injected with adenovirus carrying β-gal (lane 1) or DK-HA (lane 2). Sections of BIO14.6 hamster skeletal muscles injected with adenovirus carrying β-gal (left) or DK-HA (right) were stained with anti-TRPV2. Scale bar: 100 μm. (**B**) Skeletal muscles were stained with H&E (upper panels) or TUNEL (lower panels). Scale bar: 100 μm. (**C**) Cross-sectional areas of each individual fiber were measured and the variability of muscle fiber size was determined by averaging the standard deviations of data (upper). The number of centrally nucleated fibers was also measured using the same histological sections (middle). Number of apoptotic fibers is shown as a ratio between TUNEL labeled nuclei and total nuclei (>1000) observed in three hamsters (lower).

such as growth factors and chemotactic peptides (16,22,27). We recently reported that stretch-induced ATP release contributes to abnormal Na^+ and Ca^{2+} handlings in dystrophic muscles via the P2 receptor (28). In addition, the release of hormones such as IGF-1 and TGFβ has been well documented in dystrophic pathogenesis (28–30). The stretch signal is expected to be generated in both *mdx* and *mdx*/Tg mice. However, unexpectedly, dominant-negative TRPV2 markedly inhibited the plasma membrane retention of TRPV2 in *mdx*/Tg muscle fibers (see Figs 2B and 3A and Supplementary Material, Fig. S4 and S6), suggesting that TRPV2 activity may be required for surface localization in *mdx* muscles. In fact, we have previously shown that the removal of extracellular Ca^{2+} or stretch-activated channel inhibitor Gd^{3+} and general TRPV inhibitor ruthenium red markedly promote the internalization of TRPV2 in dystrophic myotubes (16). It is likely that the increase in local Ca^{2+} levels mediated by TRPV2 contributes to the persistent plasma membrane retention of TRPV2 in dystrophic muscles by blocking their internalization. In this regard, a recent study reported that TRPV2 may function as an endosomal Ca^{2+} release channel, which would control endosome fusion and/or endocytosis (31). Understanding the molecular mechanism of TRPV2 recycling will require further investigation and may accelerate the development of novel therapeutic strategies towards TRPV2.

We observed that the expression of dominant-negative TRPV2 itself exerts no apparent detrimental effect on the function and histological characteristics of muscles in Tg mice, suggesting a minor physiological role of TRPV2 in skeletal muscle. On the other hand, we presented evidence that TRPV2 can provide a Ca^{2+} pool, leading to the activation of CaMKII in *mdx* mice. Since the CaMKII-induced phosphorylation of histone deacetylase, together with the calcineurin/NFAT pathway, is known to

be critical for inducing skeletal muscle remodeling (32), TRPV2 may also play an important physiological role in Ca^{2+}-dependent remodeling processes during muscle injury and/or exercise. Although we do not exclude such a possible physiological role, the present findings suggest that activated TRPV2 becomes a major risk factor in dystrophic muscles.

In conclusion, the specific inhibition of TRPV2 led to a significant amelioration of muscle pathology in dystrophic animal models, and this channel is a promising therapeutic target for muscular dystrophy.

MATERIALS AND METHODS

Antibodies

Affinity-purified rabbit polyclonal anti-TRPV2 antibody was described previously (16). Other antibodies were obtained from the following sources: mouse monoclonal anti-glyceraldehyde-3-phosphate-dehydrogenase (GAPDH), rabbit polyclonal anti-TRPV1, Chemicon; mouse monoclonal anti-dystrophin, Sigma; rat anti-HA antibody (3F10), Roche; rabbit anti-GFP, Medical & Biological Laboratories co., LTD; mouse monoclonal anti-β-dystroglycan, Novocastra Laboratories, Newcastle, UK; rabbit polyclonal anti-CaMKII and anti-TRPV3, Santa Cruz Biotechnology, INC; mouse monoclonal anti-phosphorylated CaMKII, ABR Golden Co.; rabbit polyclonal anti-TRPCs (TRPC1, 3, 4 and 6)and anti-TRPV4, Alomone labs Ltd.

DNA manipulation and adenovirus production

All plasmid constructions of TRPV2 were essentially carried out by PCR-based strategy using the full-length mouse TRPV2 cDNA cloned into the pIRES expression vector (Invitrogen, Carlsbad, CA, USA). In some constructs, a HA-tag or GFP was cloned to the C-terminus of TRPV2 in pIRES or pEGFP-N1 (Clontech, Palo Alto, CA, USA) vector, respectively. GFP was inserted at the C-terminus just after the HA-tag. Three mutants were produced by substituting the conserved Glu residues (Glu594 and Glu604) of TRPV2 with Lys, either singly (E594K or E604K) or together (DK). For adenoviral gene transfer, we inserted the TRPV2 mutant cDNAs or β-gal as a control into the Adeno-X^{TM} viral vector (Clontech). Adenovirus was produced according to the manufacturer's protocol. One-day-old myotubes in differentiated medium were infected with adenoviruses at an MOI of 5–10 viral particles per cell for 24 h and cultured for an additional 36–48 h. For *in vivo* experiments, a virus aliquot was injected into right quadriceps at 5×10^9 *pfu*. Fourteen days after injection, the hamsters were subjected to experiments.

Transgenic mice

The transgene was constructed by inserting a cDNA encoding the full-length mouse TRPV2 mutant tagged with HA (E604K-HA) into the cloning site between the human α-skeletal actin promoter and the SV40 polyadenylation sequence of the plasmid [kindly provided by Dr Jeffrey S. Chamberlain (33)]. The transgene was used to generate Tg mice from C57BL/6J mice according to standard procedures. Two lines (I and II) of male F2 transgenic homozygotes were mated with female *mdx* mice. Male pups that expressed transgene were identified through PCR screening of genomic DNA extracted from tail tissue. Only the male *mdx*/Tg offspring (*mdx*/Tg I or II) were analyzed. The absence of dystrophin from these mice was confirmed by immunological detection with anti-dystrophin antibody. Genotyping was carried out by PCR with specific primers. PCR of the tail DNA was used to identify Tg mice using primers in the 3′ end of the human α-skeletal actin promoter (5′-AAGCCAAAGTCCTAATGTGC A-3′) and a sequence within TRPV2 (5′-AATGAATTCGT AGTTGAGATTCACTTTAAT-3′). Normal and abnormal dystrophin genes were detected by PCR using the following primers: sense primer, 5′-AACTCATCAAATATGCGTGTTA GTG-3′; antisense primer for normal dystrophin, GTCACTCA-GATAGTTGAAGCCATTTTAA; antisense primer for abnormal dystrophin present in *mdx* mice, GTCACTCAGATATA GTTGAAGCCATTTAG.

Animal experiments

All animal experiments were performed according to the Guidelines for Animal Experimentation at the National Cardiovascular Center. Muscle strength was evaluated by a grip-test as previously described (28). Briefly, mice were placed to hold onto a fine wire net with their forelimbs and the length of the time they could support their body weight was recorded. CK activity was measured as previously described (28).

Histology

Skeletal muscle was fixed in phosphate buffer saline (PBS) containing 10% formalin and embedded in paraffin. Serial sections (5 μm) were stained with hematoxylin and eosin (H&E) or Masson's trichrome for morphological analysis. The extent of muscle regeneration was determined by counting the number of fibers with central nuclei. The variability in fiber size was determined by averaging the standard deviations of the area from the myofiber cross-sectional views (>1000 fibers) of three to four animals per group (28). To detect apoptosis, muscle fibers were TUNEL stained using an apoptosis detection kit (Takara Biomedical). For the measurement of EBD uptake, EBD in PBS (10 mg/ml) was injected intraperitoneally into each kind of mice (0.1 ml/10 g body weight). The mice were sacrificed 24 h after injection. Muscles were excised and embedded in optimal cutting temperature compound (Tissue-Tek, Torrence, CA, USA) and snap-frozen using liquid nitrogen. Blocks were then sectioned into 6-μm thick slices, dried for 10 min and washed briefly in PBS. The EBD was detected as red auto-fluorescence. All histochemical analysis was done by investigators blinded to genotype.

Quantification of histological data

Stained serial sections were viewed under a light microscope (OLYMPUS BX41) and images were analyzed using a computer-assisted imaging system (FLOVEL Filing System) by investigators blinded to the genotypes. Images were acquired using a digital camera (Olympus FX380) equipped with image filing software (Flovel FLVFS-LS, Tokyo, Japan). The extent of damage occurring in muscles was determined by comparing the

number of centrally located nuclei (CLN) between samples. The variability of fiber size was obtained by averaging the standard deviations of cross-sectional myofiber views. Fibrosis was assessed by measuring the Masson's trichrome-positive area. Briefly, color images were converted to binary images by setting a threshold so only blue-stained fibrotic areas were detected. These areas were summed and reported as a percentage of the total area. The infiltrate area was defined as the region infiltrating non-muscle cells, such as lymphocytes and macrophages, and showing the accumulation of small nuclei and weak staining with eosin. Such areas were selected by eye and represented as the percentage of the total area.

Immunoblot and immunohistochemistry

Immunoblotting and immunohistochemistry were carried out as previously described (16,34). Briefly, the immunoblot was visualized using an enhanced chemiluminescence detection system (Amersham Biosciences) after blotting, blocking with PBS containing 5% non-fat milk and incubation with the appropriate primary and horseradish peroxidase-conjugated secondary antibodies. For immunohistochemistry, several different procedures were used. Frozen muscle sections (5–6 μm thick) or methanol fixed myotubes were double immunostained by incubating for 1 h with fluorescein isothiocyanate (FITC)-conjugated rat anti-HA antibody and rabbit anti-TRPV2 antibody, followed by further incubation with rhodamine-conjugated secondary antibody. Frozen muscle sections were also immunostained with anti-dystrophin antibody. For the immunostaining of isolated fibers, fibers immobilized on glass slides were fixed with 4% paraformaldehyde for 15 min at room temperature, permeabilized with 0.1% TritonX-100 and then stained with anti-TRPV2 antibody followed by FITC-conjugated secondary antibody. Stained samples were observed by a confocal laser scanning microscopy (FLUOVIEW FV1000, Olympus) mounted on an objective lens (Olympus). Serial sections of BIO14.6 skeletal muscles were immunostained with an enzymatic color detection system. Sections were incubated with anti-HA or anti-TRPV2 overnight, then treated with Simple Stain MAX-PO (NICHIREI CO.) for rat antibody or DAKO EnVision™+System (Peroxidase) for rabbit antibody, followed by color development with diaminobenziden (DAB). Samples were observed by a light microscope (OLYMPUS BX41).

Isolation of fibers

FDB muscles were removed and incubated for 40 min at 37°C in Krebs solution containing 124 mM NaCl, 1.2 mM $MgCl_2$, 5.9 mM KCl, 11.5 mM glucose, 11.5 mM Hepes-Na, 1.5 mM $CaCl_2$ and 0.2% collagenase type IV (Sigma-Aldrich). Muscles were then removed, washed twice in Krebs buffer and suspended in Ham's F12/DME (Sigma-Aldrich) supplemented with 2% FCS. Single fibers were mechanically dissociated by repeatedly passing the muscle through fire-polished Pasteur pipettes. Dissociated fibers were plated onto glass-bottom dishes coated with BDcell-Tak™ (BD Biosciences) and allowed to adhere to the bottom of the dish for 2 h.

Cell culture, plasmid transfection and myotube preparation

Chinese hamster ovary (CHO-K1) cells and corresponding transfectants were maintained in DMEM containing 25 mM $NaHCO_3$ and supplemented with 7.5% (v/v) fetal calf serum. cDNAs were transfected into CHO cells with Lipofectamine 2000 (Invitrogen Corp., CA, USA) and stable clones were isolated after selection with puromycin or G418. Myotube culture was performed using muscles from normal or BIO14.6 hamsters by enzymatic dissociation essentially as described previously (35). Briefly, we prepared satellite cells from the gastrocnemius muscle of hamsters using an enzyme cocktail containing 0.5 mM $CaCl_2$ for cell dissociation. After enrichment of the myoblasts by several preplatings, cells were placed on the culture dishes; 2 days later, culture medium was switched to DMEM containing 2% horse serum to induce myotube formation. Two to 4 days after start of fusion, the generated myotubes were analyzed.

Application of stretch

Myotubes were subjected to a uniaxial sinusoidal stretch of up to 120% at 1 Hz and 25°C for 1 h using a temperature-controlled stretching apparatus (NS-300; SCHOLAR-TEC Co., Osaka, Japan) as described previously (36). Cells were cultured in a silicon-rubber chamber with 400 μm thick side walls and a 200 μm thick transparent bottom coated with collagen I. In this way, uniform stretch was applied to most of cells cultured on the bottom (36). Osmotic stress-induced cell damage was observed in myofibers preloaded with 5 μM calcein-AM as previously described (15).

Ca^{2+} measurement

CHO cells and HEK293 cells were loaded with 4 μM fura-2 acetoxymethyl ester (fura-2/AM) for 30 min at 37°C, and maintained in balanced salt solution (BSS) (146 mM NaCl, 4 mM KCl, 2 mM $MgCl_2$, 0.5 mM $CaCl_2$, 10 mM glucose, 0.1% bovine serum albumin and 10 mM HEPES/Tris, pH7.4); fura-2 fluorescence was measured by a ratiometric fluorescence method using a fluorescence image processor (Aquacosmos, Hamamatsu Photonics). The excitation wavelength was alternated at 340 and 380 nm (1 Hz), and the emitted fluorescence light was detected at 510 nm. The fluorescence ratio at 340/380 nm was calculated and $[Ca^{2+}]_i$ was determined using a K_d of 135 nM for the dissociation of fura-2/Ca^{2+} complex (37). Muscle fibers were loaded for 1 h at room temperature with 4 μM fura-2/AM in BSS. For the experiments, the working medium contained 50 μM N-benzyl-p-toluene sulphonamide (BTS), an inhibitor of the myosin II ATPase. Stimulation with 2APB was performed in BSS containing 5 mM $CaCl_2$ (pH6.8). Myotubes were loaded with 4 μM fluo-4 acetoxymethyl ester for 30 min at 37°C, and maintained in BSS. Fluorescence signal was detected with a confocal microscope (MRC-1024; Bio-Rad, Richmond, CA, USA) mounted on an Olympus BX50WI microscope. Images were acquired at a rate of one image every 1 s and single-frames or the single cell-integrated signal density were analyzed by Laser-Sharp software (Bio-Rad). All Ca^{2+} measurements were carried out at room temperature.

Statistical analysis

Unless otherwise stated, data are represented as means ± SD of at least three determinations. We used an unpaired *t*-test, one-way analysis of variance followed by Dunnett's test for statistical analyses. Values of $P < 0.05$ (indicated as asterisks in figures) were considered statistically significant.

SUPPLEMENTARY MATERIAL

Supplementary Material is available at *HMG* Online.

ACKNOWLEDGEMENTS

We thank Ms H. Otake for her technical assistance.

Conflict of Interest statement. None declared.

FUNDING

This work was supported by Grant-in-Aid for Priority Areas 18077015 (to S.W.), Grants-in-Aid 19390080, 17659241 (to S.W.), 18590796 (Y.I.) and a Grant for the Cooperative Link for Unique Science and Technology for Economy Revitalization (S.W.) from the Ministry of Education, Culture, Sports, Science and Technology of Japan, a grant for the Promotion of Fundamental Studies in Health Sciences of National Institute of Biomedical Innovation (NIBIO), research grants for Cardiovascular Diseases (17A-1) (S.W.) and for Nervous and Mental Disorders (16B-2 and 19A-7) from the Ministry of Health, Labor, and Welfare (to Y.I.), and grants from Takeda Science Foundation (to Y.I.) and the Salt Science Research Foundation, No. 0737 (to S.W.).

REFERENCES

1. Duclos, F., Straub, V., Moore, S.A., Venzke, D.P., Hrstka, R.F., Crosbie, R.H., Durbeej, M., Lebakken, C.S., Ettinger, A.J., van der Meulen, J. *et al.* (1998) Progressive muscular dystrophy in alpha-sarcoglycan-deficient mice. *J. Cell Biol.*, **142**, 1461–1471.
2. Campbell, K.P. (1995) Three muscular dystrophies: loss of cytoskeleton-extracellular matrix linkage. *Cell*, **80**, 675–679.
3. Nigro, V., Okazaki, Y., Belsito, A., Piluso, G., Matsuda, Y., Politano, L., Nigro, G., Ventura, C., Abbondanza, C., Molinari, A.M. *et al.* (1997) Identification of the Syrian hamster cardiomyopathy gene. *Hum. Mol. Genet.*, **6**, 601–607.
4. Campbell, K.P. and Kahl, S.D. (1989) Association of dystrophin and an integral membrane glycoprotein. *Nature*, **338**, 259–262.
5. Tinsley, J.M., Blake, D.J., Zuellig, R.A. and Davies, K.E. (1994) Increasing complexity of the dystrophin-associated protein complex. *Proc. Natl Acad. Sci. USA*, **91**, 8307–8313.
6. Ervasti, J.M. and Campbell, K.P. (1993) A role for the dystrophin–glycoprotein complex as a transmembrane linker between laminin and actin. *J. Cell Biol.*, **122**, 809–823.
7. Turner, P.R., Westwood, T., Regen, C.M. and Steinhardt, R.A. (1988) Increased protein degradation results from elevated free calcium levels found in muscle from mdx mice. *Nature*, **335**, 735–738.
8. Spencer, M.J., Croall, D.E. and Tidball, J.G. (1995) Calpains are activated in necrotic fibers from mdx dystrophic mice. *J. Biol. Chem.*, **270**, 10909–10914.
9. MacLennan, P.A., McArdle, A. and Edwards, R.H. (1991) Effects of calcium on protein turnover of incubated muscles from mdx mice. *Am. J. Physiol.*, **260**, E594–E598.
10. Mallouk, N., Jacquemond, V. and Allard, B. (2000) Elevated subsarcolemmal Ca^{2+} in mdx mouse skeletal muscle fibers detected with Ca^{2+}-activated K^+ channels. *Proc. Natl Acad. Sci. USA*, **97**, 4950–4955.
11. Robert, V., Massimino, M.L., Tosello, V., Marsault, R., Cantini, M., Sorrentino, V. and Pozzan, T. (2001) Alteration in calcium handling at the subcellular level in mdx myotubes. *J. Biol. Chem.*, **276**, 4647–4651.
12. Fong, P.Y., Turner, P.R., Denetclaw, W.F. and Steinhardt, R.A. (1990) Increased activity of calcium leak channels in myotubes of Duchenne human and mdx mouse origin. *Science*, **250**, 673–676.
13. Nakamura, T.Y., Iwata, Y., Sampaolesi, M., Hanada, H., Saito, N., Artman, M., Coetzee, W.A. and Shigekawa, M. (2001) Stretch-activated cation channels in skeletal muscle myotubes from sarcoglycan-deficient hamsters. *Am. J. Physiol. Cell Physiol.*, **281**, C690–C699.
14. Vandebrouck, C., Martin, D., Colson-Van Schoor, M., Debaix, H. and Gailly, P. (2002) Involvement of TRPC in the abnormal calcium influx observed in dystrophic (mdx) mouse skeletal muscle fibers. *J. Cell Biol.*, **158**, 1089–1096.
15. Iwata, Y., Katanosaka, Y., Shijun, Z., Kobayashi, Y., Hanada, H., Shigekawa, M. and Wakabayashi, S. (2005) Protective effects of Ca^{2+} handling drugs against abnormal Ca^{2+} homeostasis and cell damage in myopathic skeletal muscle cells. *Biochem. Pharmacol.*, **70**, 740–751.
16. Iwata, Y., Katanosaka, Y., Arai, Y., Komamura, K., Miyatake, K. and Shigekawa, M. (2003) A novel mechanism of myocyte degeneration involving the Ca^{2+}-permeable growth factor-regulated channel. *J. Cell Biol.*, **161**, 957–967.
17. Nilius, B., Owsianik, G., Voets, T. and Peters, J.A. (2007) Transient receptor potential cation channels in disease. *Physiol. Rev.*, **87**, 165–217.
18. Venkatachalam, K. and Montell, C. (2007) TRP channels. *Annu. Rev. Biochem.*, **76**, 387–417.
19. Clapham, D.E., Julius, D., Montell, C. and Schultz, G. (2005) International Union of Pharmacology. XLIX. Nomenclature and structure-function relationships of transient receptor potential channels. *Pharmacol. Rev.*, **57**, 427–450.
20. Nilius, B., Vennekens, R., Prenen, J., Hoenderop, J.G., Droogmans, G. and Bindels, R.J. (2001) The single pore residue Asp542 determines Ca^{2+} permeation and Mg^{2+} block of the epithelial Ca^{2+} channel. *J. Biol. Chem.*, **276**, 1020–1025.
21. Garcia-Martinez, C., Morenilla-Palao, C., Planells-Cases, R., Merino, J.M. and Ferrer-Montiel, A. (2000) Identification of an aspartic residue in the P-loop of the vanilloid receptor that modulates pore properties. *J. Biol. Chem.*, **275**, 32552–32558.
22. Kanzaki, M., Zhang, Y.Q., Mashima, H., Li, L., Shibata, H. and Kojima, I. (1999) Translocation of a calcium-permeable cation channel induced by insulin-like growth factor-I. *Nat. Cell Biol.*, **1**, 165–170.
23. Wehling, M., Spencer, M.J. and Tidball, J.G. (2001) A nitric oxide synthase transgene ameliorates muscular dystrophy in mdx mice. *J. Cell Biol.*, **155**, 123–131.
24. Garcia-Sanz, N., Fernandez-Carvajal, A., Morenilla-Palao, C., Planells-Cases, R., Fajardo-Sanchez, E., Fernandez-Ballester, G. and Ferrer-Montiel, A. (2004) Identification of a tetramerization domain in the C terminus of the vanilloid receptor. *J. Neurosci.*, **24**, 5307–5314.
25. Hellwig, N., Albrecht, N., Harteneck, C., Schultz, G. and Schaefer, M. (2005) Homo- and heteromeric assembly of TRPV channel subunits. *J. Cell Sci.*, **118**, 917–928.
26. Lee, E.H., Kim do, H. and Allen, P.D. (2006) Interplay between intra- and extracellular calcium ions. *Mol. Cells*, **21**, 315–329.
27. Nagasawa, M., Nakagawa, Y., Tanaka, S. and Kojima, I. (2007) Chemotactic peptide fMetLeuPhe induces translocation of the TRPV2 channel in macrophages. *J. Cell. Physiol.*, **210**, 692–702.
28. Iwata, Y., Katanosaka, Y., Hisamitsu, T. and Wakabayashi, S. (2007) Enhanced Na^+/H^+ exchange activity contributes to the pathogenesis of muscular dystrophy via involvement of P2 receptors. *Am. J. Pathol.*, **171**, 1576–1587.
29. Perrone, C.E., Fenwick-Smith, D. and Vandenburgh, H.H. (1995) Collagen and stretch modulate autocrine secretion of insulin-like growth factor-1 and insulin-like growth factor binding proteins from differentiated skeletal muscle cells. *J. Biol. Chem.*, **270**, 2099–2106.
30. Fadic, R. (2005) Cell surface and gene expression regulation molecules in dystrophinopathy: mdx vs. Duchenne. *Biol. Res.*, **38**, 375–380.
31. Saito, M., Hanson, P.I. and Schlesinger, P. (2007) Luminal chloride-dependent activation of endosome calcium channels: patch clamp study of enlarged endosomes. *J. Biol. Chem.*, **282**, 27327–27333.
32. Bassel-Duby, R. and Olson, E.N. (2006) Signaling pathways in skeletal muscle remodeling. *Annu. Rev. Biochem.*, **75**, 19–37.

33. Crawford, G.E., Faulkner, J.A., Crosbie, R.H., Campbell, K.P., Froehner, S.C. and Chamberlain, J.S. (2000) Assembly of the dystrophin-associated protein complex does not require the dystrophin COOH-terminal domain. *J. Cell Biol.*, **150**, 1399–1410.
34. Iwata, Y., Pan, Y., Hanada, H., Yoshida, T. and Shigekawa, M. (1996) Dystrophin–glycoprotein complex purified from hamster cardiac muscle. Comparison of the complexes from cardiac and skeletal muscles of hamster and rabbit. *J. Mol. Cell. Cardiol.*, **28**, 2501–2509.
35. Rando, T.A. and Blau, H.M. (1994) Primary mouse myoblast purification, characterization, and transplantation for cell-mediated gene therapy. *J. Cell Biol.*, **125**, 1275–1287.
36. Naruse, K., Yamada, T. and Sokabe, M. (1998) Involvement of SA channels in orienting response of cultured endothelial cells to cyclic stretch. *Am. J. Physiol.*, **274**, H1532–H1538.
37. Grynkiewicz, G., Poenie, M. and Tsien, R.Y. (1985) A new generation of Ca^{2+} indicators with greatly improved fluorescence properties. *J. Biol. Chem.*, **260**, 3440–3450.

Biophysical Journal Volume 97 November 2009 2674–2683

A Model of Na^+/H^+ Exchanger and Its Central Role in Regulation of pH and Na^+ in Cardiac Myocytes

Chae Young Cha,[†‡] Chiaki Oka,[‡] Yung E. Earm,[§] Shigeo Wakabayashi,[¶] and Akinori Noma[†*]

[†]Biosimulation Project, Faculty of Bioinformatics, Ritsumeikan University, Kusatsu, Japan; [‡]Biosimulation Project, Graduate School of Medicine, Kyoto University, Kyoto, Japan; [§]Department of Physiology, Seoul National University, Seoul, Korea; and [¶]Department of Molecular Physiology, National Cardiovascular Center Research Institute, Osaka, Japan

ABSTRACT A new kinetic model of the Na^+/H^+ exchanger (NHE) was developed by fitting a variety of major experimental findings, such as ion-dependencies, forward/reverse mode, and the turnover rate. The role of NHE in ion homeostasis was examined by implementing the NHE model in a minimum cell model including intracellular pH buffer, Na^+/K^+ pump, background H^+, and Na^+ fluxes. This minimum cell model was validated by reconstructing recovery of pH_i from acidification, accompanying transient increase in $[Na^+]_i$ due to NHE activity. Based on this cell model, steady-state relationships among pH_i, $[Na^+]_i$, and $[Ca^{2+}]_i$ were quantitatively determined, and thereby the critical level of acidosis for cell survival was predicted. The acidification reported during partial blockade of the Na^+/K^+ pump was not attributed to a dissipation of the Na^+ gradient across the membrane, but to an increase in indirect H^+ production. This NHE model, though not adapted to the dimeric behavioral aspects of NHE, can provide a strong clue to quantitative prediction of degree of acidification and accompanying disturbance of ion homeostasis under various pathophysiological conditions.

INTRODUCTION

Several types of pH-related transporters are present in the sarcolemma of cardiac myocytes. Among them, the Na^+-H^+ exchanger (NHE) is regarded as the main acid extruder, in that its H^+ flux is much larger than that of the other acid extruder, the Na^+-HCO_3^- cotransporter (1,2). In addition, abnormal enhancement of NHE activity under acidosis potentially induces intracellular Na^+ overload through Na^+ influx during pumping out excess H^+ (3) and eventually Ca^{2+} overload by depressing the Na^+-Ca^{2+} exchanger (NCX). For example, the enhanced NHE has been reported to play a critical role in ischemia/reperfusion injury (4,5), and slow force response (6,7). Since regulation of all intracellular H^+, Na^+, and Ca^{2+} concentrations within a physiological range is of vital importance in maintaining the excitability, contractility, and cell volume regulation in cardiac myocytes, a dynamic NHE model is indispensable to investigate mechanisms underlying the cellular ionic homeostasis as well as its failure under pathophysiological conditions using mathematical cell models.

A variety of mathematical models of NHE has been developed. Leem et al. (1) derived an empirical polynomial equation based on their measurements of pH_i-NHE flux relationships, and this model was used for exploring effects of acidosis on contraction and membrane excitation (8,9). NHE activity has also been described with Hill equations (10) or by a simple kinetic model (11) that attributed NHE activation to binding of intracellular H^+ to its modifier site. These simple models were easy to apply, but did not provide any details of the dependencies on the intra- and extracellular concentrations of H^+ and Na^+, except for pH_i. Recently, more-complicated kinetic NHE models have been proposed (12–15), but even the latest NHE model (14) did not take account of extracellular H^+ or Na^+ dependencies. In addition to these classical NHE schemes, model development based on the dimer configuration of NHE (16) has been attempted (17–20). However, these models are quite different from each other and it is still difficult to distinguish them experimentally. Furthermore, in cardiac myocytes no positive proof is demonstrated for the cooperative operation of monomers within the dimeric composition. Thus, there is no available NHE model with sufficient detail to predict the contribution of NHE in intact myocytes.

In this study, we developed an NHE model, which satisfactorily reconstructs the dependencies on the intra- and extracellular concentrations of H^+ and Na^+ reported in the systematic experiments in the Purkinje fiber (21,22), in addition to the experimental findings in the transfected cell line (15). Subsequently, we implemented the new NHE model in a simple cell model, and found that original recordings of pH_i and $[Na^+]_i$ variations in experiments were well explained by the alteration of NHE activity. We then examined the role of NHE under pathophysiological conditions by considering the steady-state relationship between pH_i and $[Na^+]_i$ during depression of active Na^+ transport or during long-lasting acidosis.

METHODS

Development of the NHE model scheme

A variety of kinetic schemes, such as ping-pong (12,13), simultaneous ion-transporting (17,18), or dimer models (19,20) have been suggested for NHE. These model schemes might equally well explain experimental findings.

Submitted November 5, 2008, and accepted for publication August 21, 2009.

*Correspondence: noma@sk.ritsumei.ac.jp

Editor: Michael Pusch.

0006-3495/09/11/2674/10 $2.00

doi: 10.1016/j.bpj.2009.08.053

Because of its applicability to a wide range of experimental data, we adopted a ping-pong scheme with 1:1 stoichiometry. Consideration of the dimeric model schemes is presented in the Supporting Material.

The new kinetic NHE model is composed of two distinct functional units: an ion-exchanging part (j_{exch}) and a proton-modifier part (*Mod*). The H^+ efflux or Na^+ influx through NHE (J_{NHE}) is given by the equation

$$J_{NHE}(\text{mM/ms}) = N \times Mod([H^+]_i, [H^+]_o) \times j_{exch}([H^+]_i, [H^+]_o, [Na^+]_i, [Na^+]_o)/(A\, vol_i), \quad (1)$$

where N is the total number of NHE molecules, A is the Avogadro number, and vol_i is the intracellular volume.

The ion-exchanging part (j_{exch})

A ping-pong-type model with $1H^+$:$1Na^+$ stoichiometry (23) can be described with a six- or eight-state model (Fig. 1, *A* or *B*) by assuming that H^+ and Na^+ either can or cannot bind simultaneously to the transporter (23). In the six-state model, the steady-state turnover rate, j_{exch}, is given as

$$j_{exch} = \frac{\dfrac{k_1^+\frac{[Na^+]_o}{K_{Na}^o}}{\left(1+\frac{[Na^+]_o}{K_{Na}^o}+\frac{[H^+]_o}{K_H^o}\right)}\dfrac{k_2^+\frac{[H^+]_i}{K_H^i}}{\left(1+\frac{[Na^+]_i}{K_{Na}^i}+\frac{[H^+]_i}{K_H^i}\right)} - \dfrac{k_1^-\frac{[Na^+]_i}{K_{Na}^i}}{\left(1+\frac{[Na^+]_i}{K_{Na}^i}+\frac{[H^+]_i}{K_H^i}\right)}\dfrac{k_2^-\frac{[H^+]_o}{K_H^o}}{\left(1+\frac{[Na^+]_o}{K_{Na}^o}+\frac{[H^+]_o}{K_H^o}\right)}}{\dfrac{k_1^+\frac{[Na^+]_o}{K_{Na}^o}}{\left(1+\frac{[Na^+]_o}{K_{Na}^o}+\frac{[H^+]_o}{K_H^o}\right)}+\dfrac{k_2^+\frac{[H^+]_i}{K_H^i}}{\left(1+\frac{[Na^+]_i}{K_{Na}^i}+\frac{[H^+]_i}{K_H^i}\right)}+\dfrac{k_1^-\frac{[Na^+]_i}{K_{Na}^i}}{\left(1+\frac{[Na^+]_i}{K_{Na}^i}+\frac{[H^+]_i}{K_H^i}\right)}+\dfrac{k_2^-\frac{[H^+]_o}{K_H^o}}{\left(1+\frac{[Na^+]_o}{K_{Na}^o}+\frac{[H^+]_o}{K_H^o}\right)}}. \quad (2)$$

In the eight-state model, it is given as

$$j_{exch} = \frac{\dfrac{k_1^+\frac{[Na^+]_o}{K_{Na}^o}}{\left(1+\frac{[Na^+]_o}{K_{Na}^o}\right)\left(1+\frac{[H^+]_o}{K_H^o}\right)}\dfrac{k_2^+\frac{[H^+]_i}{K_H^i}}{\left(1+\frac{[Na^+]_i}{K_{Na}^i}\right)\left(1+\frac{[H^+]_i}{K_H^i}\right)} - \dfrac{k_1^-\frac{[Na^+]_i}{K_{Na}^i}}{\left(1+\frac{[Na^+]_i}{K_{Na}^i}\right)\left(1+\frac{[H^+]_i}{K_H^i}\right)}\dfrac{k_2^-\frac{[H^+]_o}{K_H^o}}{\left(1+\frac{[Na^+]_o}{K_{Na}^o}\right)\left(1+\frac{[H^+]_o}{K_H^o}\right)}}{\dfrac{k_1^+\frac{[Na^+]_o}{K_{Na}^o}}{\left(1+\frac{[Na^+]_o}{K_{Na}^o}\right)\left(1+\frac{[H^+]_o}{K_H^o}\right)}+\dfrac{k_2^+\frac{[H^+]_i}{K_H^i}}{\left(1+\frac{[Na^+]_i}{K_{Na}^i}\right)\left(1+\frac{[H^+]_i}{K_H^i}\right)}+\dfrac{k_1^-\frac{[Na^+]_i}{K_{Na}^i}}{\left(1+\frac{[Na^+]_i}{K_{Na}^i}\right)\left(1+\frac{[H^+]_i}{K_H^i}\right)}+\dfrac{k_2^-\frac{[H^+]_o}{K_H^o}}{\left(1+\frac{[Na^+]_o}{K_{Na}^o}\right)\left(1+\frac{[H^+]_o}{K_H^o}\right)}}, \quad (3)$$

where k values are rate constants and the K values are dissociation constants for individual ions. It is assumed that the binding and release of ions are instantaneous, and K values are not affected by binding of Na^+ or H^+ in the eight-state model.

The proton-modifier part (Mod)

Distinct from the ion-exchanging mechanism, NHE has an intracellular H^+-binding step for its activation (15). Since the value of the Hill coefficient (n_H) is still a matter of debate (24,25), we tested n_H values from 1 to 4 in data fitting of a Hill equation:

$$Mod = \frac{1}{1+\dfrac{(K_i)^{n_H}}{([H^+]_i)^{n_H}}}. \quad (4)$$

The pH_i-J_{NHE} relationship shifted in the acidic pH_i direction with decreasing pH_o in cardiac myocytes (21,22,26) and other cell types (24,27). However, the mechanism of depression by the extracellular H^+ has not been determined experimentally. Two mechanisms were considered here. First, the parallel shift may simply result from a competitive interaction between extracellular H^+ and Na^+ in the ion-exchanging part (24). In this case, the *Mod* remains the same as described by Eq. 4. Secondly, the parallel shift might occur when the extracellular H^+ directly modulates the proton-modifier part (Fig. 1 *C*), as expressed by

$$Mod = \frac{1}{1+\left(1+\dfrac{([H^+]_o)^{m_H}}{(K_o)^{m_H}}\right)\dfrac{(K_i)^{n_H}}{([H^+]_i)^{n_H}}}. \quad (5)$$

Mod in the former scheme is designated as *Mod1* (Eq. 4) and the latter as *Mod2* (Eq. 5). The Hill coefficient for extracellular H^+ (m_H) was

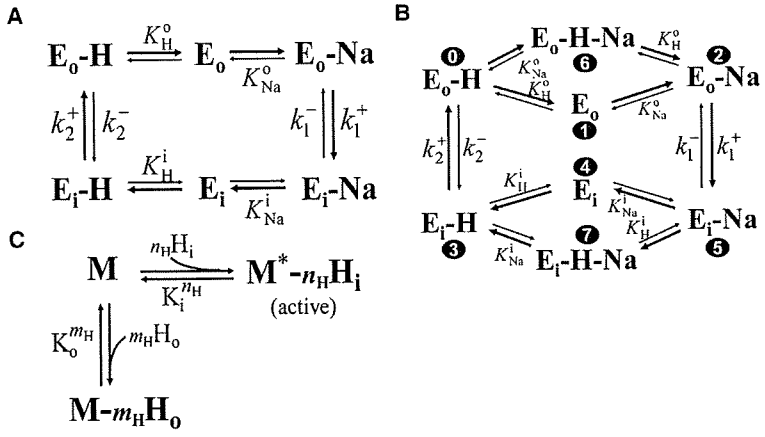

FIGURE 1 Schemes for the NHE model. Schemes for the ion-exchanging part: the six-state model (*A*) and the eight-state model (*B*). E_o represent the state in which the binding cavity opens to the outside of the cell and E_i is the state with the binding cavity open to the inside. The thick arrows indicate the forward direction. Definitions of the parameters are given in Table S1. The numerals in panel *B* indicate state labels that are referred to in Fig. 9 *B*. (*C*) Schemes for the proton-modifier part (M). Ion binding was assumed to be instantaneous with equilibrium constants, the *K* values. The asterisk indicates the state of M that activates E.

assumed to be 1 in this study, based on the experimental finding of $m_H = 1.2$ (21).

When the experimental data were fitted with Eq. 1, j_{exch} of a six- (Eq. 2) or eight-state (Eq. 3) model and *Mod1* (Eq. 4) or *Mod2* (Eq. 5) were examined. Since n_H ranged from 1 to 4, we examined 16 combinations of j_{exch} and *Mod* by data fitting.

Determination of unknown parameters

The ion-exchanging part of the NHE model was expressed as a closed-loop and constrained by the following microscopic reversibility (Eq. 6), leaving nine or 10 unknown parameters to be determined (see Table S1 in the Supporting Material):

$$\frac{K_H^i K_{Na}^o}{K_H^o K_{Na}^i} = \frac{k_1^+ k_2^+}{k_1^- k_2^-}. \quad (6)$$

Methods of fitting

The Levenberg-Marquardt fitting method was used to search for a minimum of chi-square (χ^2),

$$\chi^2 = \sum_{m=1}^{M} \left(\frac{y_m - y(x_m)}{\sigma_m} \right)^2, \quad (7)$$

where M is size of data set, y_m is experimental data of J_{NHE}, $y(x_m) = J_{NHE}([H^+]_i, [H^+]_o, [Na^+]_i$, or $[Na^+]_o)$ defined by Eq. 1 and σ_m is standard deviation (SD) for the m^{th} data point. We found that the χ^2 function of J_{NHE} had numerous local minimums in 9- or 10-dimensional parameter space. Therefore, local minimums were searched with initial values which were varied systematically within a physiological range (see Table S1), and then the least χ^2 was selected among them. The interval for varying initial values should be small enough to avoid missing the global minimum of the χ^2 function. As a compromise with computational cost, 3,674,160 starting points were used in each model scheme. Further consideration of the fitting method was presented in the Supporting Material.

Experimental data for determining model parameters

Selection of relevant experimental data is critical for constructing a precise model. We used three kinds of experimental data: the amplitude of J_{NHE} at various combinations of ($[H^+]_i$, $[H^+]_o$, $[Na^+]_i$, or $[Na^+]_o$), forward/reverse mode of ionic exchange, and the NHE turnover rate.

The measurements of NHE vary due to recording techniques (ion selective electrode or fluorescent dye) or differences in specimens (species (2), and muscles or isolated cells (28)). To minimize the experimental variations, systematic data were collected in sheep Purkinje fibers from two articles published by the same group (21,22) in which their established experimental methods were used. Alternatively, the experimental data from single ventricular myocytes might be adopted. As far as we compared, however, the configuration of pH_i-, pH_o-, and $[Na^+]_o$-J_{NHE} relationships obtained in dissociated ventricular myocyte were largely comparable to those in Purkinje fiber (see the Supporting Material). Furthermore, no measurement of $[Na^+]_i$-J_{NHE} relationship was available in ventricular myocytes. Therefore, we considered that the use of Purkinje fiber data was appropriate.

Despite the identical experimental methods in Purkinje fibers, NHE flux was still quite variable among different preparations. To fit the data set simultaneously, the amplitude of J_{NHE} was normalized with reference to common pH_i, pH_o, $[Na^+]_i$, and $[Na^+]_o$ in individual results. We assumed that the major subtype was NHE1 in Purkinje fibers (29) and that the diversity of NHE flux was mainly due to different sizes of tissue preparations. Finally, the data set of ion dependencies consisted of 106 data points ($M = 106$ in Eq. 7), shown in Fig. 3 *A* and Fig. 4, *A* and *B*, which include a few invisible points. To calculate χ^2, all variables in Eq. 1 and SD were

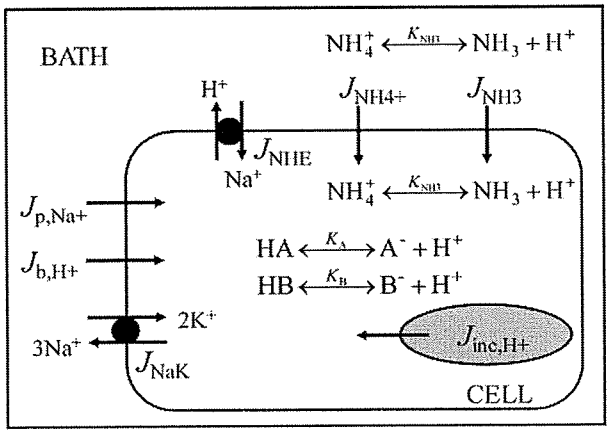

FIGURE 2 Simple cell model of cardiac Purkinje fibers. Abbreviations: $J_{p,Na+}$, passive flux of Na^+; $J_{b,H+}$, background H^+ flux; J_{NHE}, H^+ efflux or Na^+ influx through NHE; J_{NaK}, Na^+ efflux through the Na^+/K^+ pump; J_{NH3} and J_{NH4+}, passive fluxes of NH_3 and NH_4^+; and $J_{inc,H+}$, extra flux for intracellular H^+ increase by an unknown mechanism, which appears in Fig. 7. A^-, B^-, HA, and HB, free or H^+-bounded forms of intrinsic buffer species, A and B.

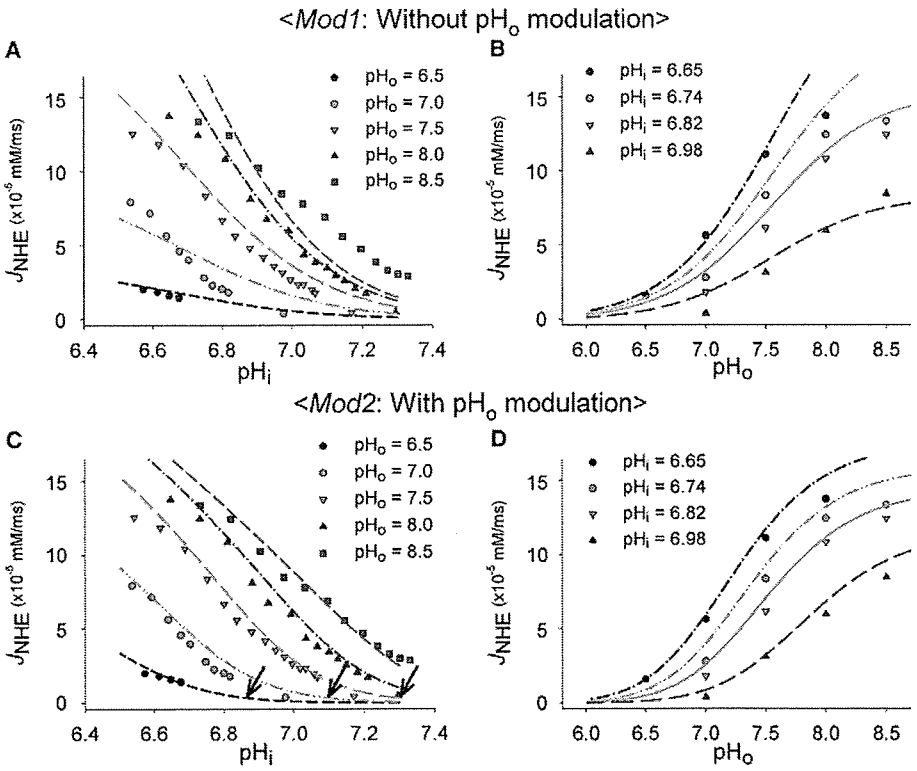

FIGURE 3 Comparison between *Mod1* and *Mod2* in response to pH_o variation. Experimental data (*symbols*) were taken from Vaughan-Jones and Wu (21). Various curves were plotted with the best fitting results for *Mod1* (*A* and *B*) or *Mod2* (*C* and *D*). Data points in panels *B* or *D* were selected from those in panels *A* or *C* for corresponding pH_i and pH_o, respectively. The arrows in panel *C* were fitted by eye to denote the location of each activation foot in the pH_i-NHE relationship at $pH_o = 6.5$, 7.0, and 7.5, respectively. Although data points were fitted with different $[Na^+]_i$, an average $[Na^+]_i$ was used to draw a continuous curve. This approximation may be justified, as the $[Na^+]_i$-J_{NHE} relation is shallow.

required, but $[Na^+]_i$ or SD was not always given in the literature. Therefore, $[Na^+]_i$ was supplemented from preliminary whole-cell simulations, and the ratio between SD and the mean of J_{NHE} described in the literature (25,30) was used for obtaining SD.

The forward/reverse mode of exchange was investigated in NHE1-transfected cells by measuring $^{22}Na^+$ flux (15). The forward mode offered information about the saturation of NHE activity at acidic pH_i below 5.2. The reverse mode provided important evidence that NHE includes a proton-

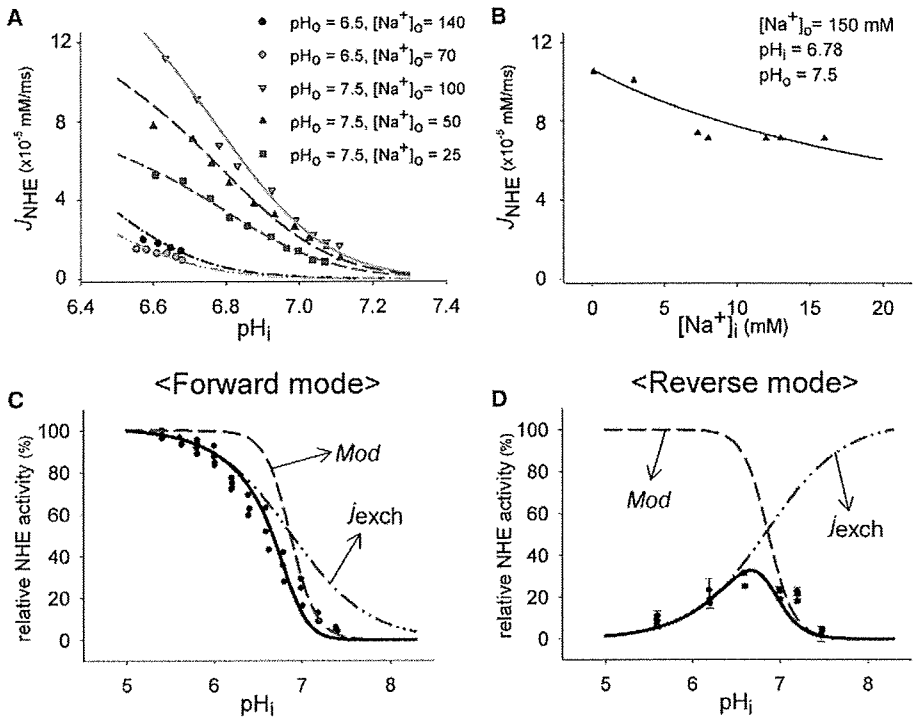

FIGURE 4 Best-fit results for NHE activity with *Mod2*. The data points in panels *A* and *B* (*symbols*) were taken from Wu and Vaughan-Jones (22). (*A*) pH_i-NHE relationship at various $[Na^+]_o$ and pH_o. As with Fig. 3, an average $[Na^+]_i$ was used to draw a continuous curve. (*B*) $[Na^+]_i$-NHE relationship. (*C* and *D*) The activities in the forward/reverse mode were simulated for $[Na^+]_i$ /$[Na^+]_o = 0$ / 1 or 1 / 0 mM, based on the experimental studies (15). The J_{NHE} curves (*bold lines*) were determined from the product of j_{exch} and *Mod* (Eq. 1).

modifier part in addition to ion-exchanging part, and helped us to determine j_{exch} and *Mod* separately. The turnover rate was measured by dividing J_{NHE} by total number of NHE molecules in experiments (31,32), which correspond to (*Mod* × j_{exch}) in Eq. 1. The turnover rate of one NHE1 molecule is 2–10 ms^{-1} at $pH_i = 6.0$, $pH_o = 7.4$, $[Na^+]_i$ ~0, and $[Na^+]_o = 140$ mM. We restricted this value to 2.3–2.5 ms^{-1} to avoid redundancies in the fitting results due to the inverse relationship between N and k values (refer to Eqs. 1–3).

Construction of a simple cell model

When pH_i recovers from acidification, $[Na^+]_i$ concurrently increases due to Na^+ influx through NHE. To check whether the experimental increase of $[Na^+]_i$ during pH_i recovery is attributable to the NHE activity, we incorporated the new NHE model into a simple cell model including the minimum components involved in pH_i or $[Na^+]_i$ regulation (Fig. 2). NBC and Cl^--HCO_3^- exchange were not considered because they are almost inactive in a HEPES-buffered system (1). A contribution of Cl^--OH^- exchange was included in a passive H^+ flux.

The equations for individual components are presented in the Appendix. For intracellular pH buffer (Eqs. 22–25), two intrinsic buffering species, A and B, were assumed. The total concentration and dissociation constants of A and B were determined based on the measurement of intrinsic pH buffering power in Purkinje fibers (33) (see the Supporting Material). Passive Na^+ flux (Eq. 13) is expressed by a constant field equation. The pH_i drift in Fig. 5 and Fig. 6 *B* in the absence of external Na^+ might be attributed to a background H^+. This flux seems to be larger at lower pH_o or at higher pH_i, and reversed to efflux at excessive acidic pH_i (22). Although Cl^--OH^- exchange is the potential candidate for the background H^+ flux in the CO_2/HCO_3^- free conditions (34,35), other unknown mechanisms might participate. Equation 14 is used only to describe the pH_i drift of unknown nature to complete the model fitting, but is not related to biophysical mechanisms. The equation for the Na^+/K^+ pump (Eq. 15) was adopted from the Kyoto model (36). We described flux of NH_4^+ with the constant field equation (Eq. 16) under the assumption that NH_4^+ is mainly transported through inwardly rectifying K^+ channels in cardiac myocytes (37). The NH_4^+ flux through Na^+/K^+ pump (38) or NHE (12) is neglected here, because the speed of acidification during NH_4Cl pulse is almost identical irrespective of the existence of Na^+ ion in intra-/extracellular medium (Fig. 5), which might affect NH_4^+ transport through Na^+/K^+ pump or NHE. Flux of NH_3 (Eq. 17) was expressed with Fick's law. The $[K^+]_i$ was set to be constant, assuming that K^+ permeability was dominant over others. For the same reason, the membrane potential was fixed at the K^+ equilibrium potential. This approximation is justified, since changes in the flux of Na^+ or NH_4^+ were small when the membrane potential was altered by $< \pm 10$ mV around the resting potential. The extracellular ionic composition was the same as that used in the experimental studies.

RESULTS

Determination of the NHE model scheme and parameters

The least χ^2 for the 16 model schemes were compared for different n_H values (see Table S2). Relatively large values were obtained with $n_H = 1$ for both *Mod1* and *Mod2*. However, it was difficult to determine which among $n_H = 2$, 3, and 4 was appropriate because of the marginal differences in χ^2. For the same reason, the six- and eight-state models of j_{exch} could not be differentiated.

A more careful approach than simple comparison of χ^2 was required to discriminate *Mod1* and *Mod2* because these

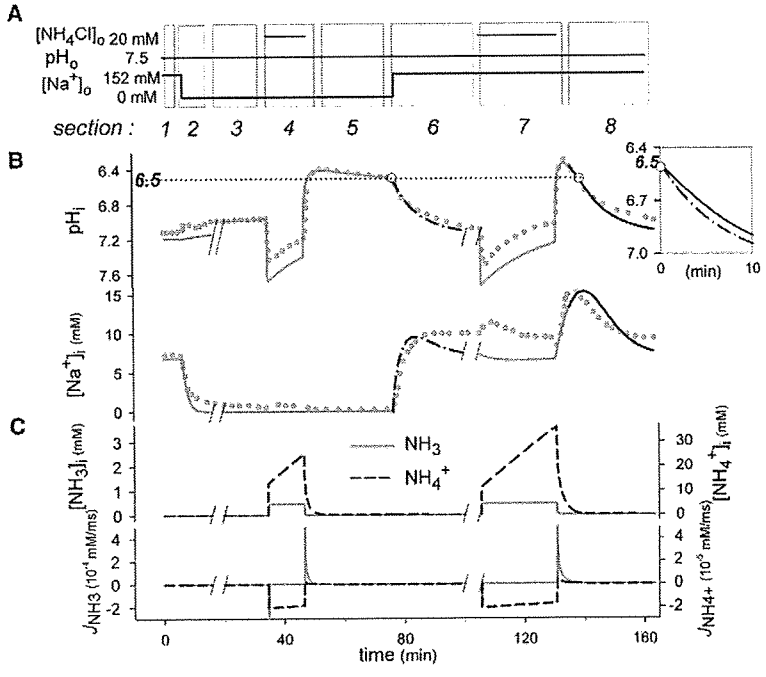

FIGURE 5 Simulation of pH_i and $[Na^+]_i$ variations in an NH_4Cl prepulse experiment. The original experimental recordings were from Fig. 5 in Wu and Vaughan-Jones (22). (*A*) The experimental protocol. (*B*) Changes of pH_i and $[Na^+]_i$ in the experiment (*shaded dots*) and in simulation (*lines*). (*Inset*) Comparison of the two recovery speeds at pH_i 6.5 between sections 6 and 8 in the simulation. Open circles indicate the time of comparison, which is indicated by a horizontal dotted line. The slash (//) denotes interruption of the simulation. (*C*) Simulated changes of $[NH_3]_i$, $[NH_4^+]_i$, J_{NH3}, and J_{NH4+}. ***Simulation of the response to an NH_4Cl prepulse***: The initial alkaline shift of pH_i was due to the almost instantaneous redistribution of NH_3 and the following relaxation is attributable to delayed accumulation of NH_4^+ within the cell. The subsequent sudden drop to pH_i 6.5 after removal of NH_4Cl was driven by the immediate and large efflux of NH_3. ***Determination of parameters for the cell model***: Cellular parameters were uniquely determined from the appropriate sections. $J_{b,H+}$ (Eq. 14) was determined from the slope of the pH change in sections 3 and 5, in which the other components were inactive due to the absence of Na^+. The amplitude of J_{NHE} (*N*) was determined by the recovery rate of pH_i in sections 8, where variation of $[Na^+]_i$ above 8 mM has little effect on NHE activity (22). J_{NaK} (*D* in Eq. 15) and $J_{p,Na+}$ (P_{Na+} in Eq. 13) were evaluated from the variations of $[Na^+]_i$ in sections 1 and 2. The parameters of J_{NH3} and J_{NH4+} (P_{NH3}, P_{NH4+} in Eqs. 16 and 17) were derived from section 4. P_{NH3} was determined by fitting the initial rising and final falling phase of pH_i record during NH_4Cl pulse, and P_{NH4+} from the slow acidification during the pulse and the rebound at the end of the pulse. P_{NH3} and P_{NH4+} had values comparable to those in previous simulation studies (46,47), if converted with a usual surface/volume ratio (36). The acid dissociation constant of NH_3/NH_4^+ (K_{NH3}) is 7.08×10^{-7} mM. We failed to avoid the small deviation of pH_i during NH_4Cl pulse when this common K_{NH3} was used for intracellular and extracellular medium. The values of model components are given in Table S3.

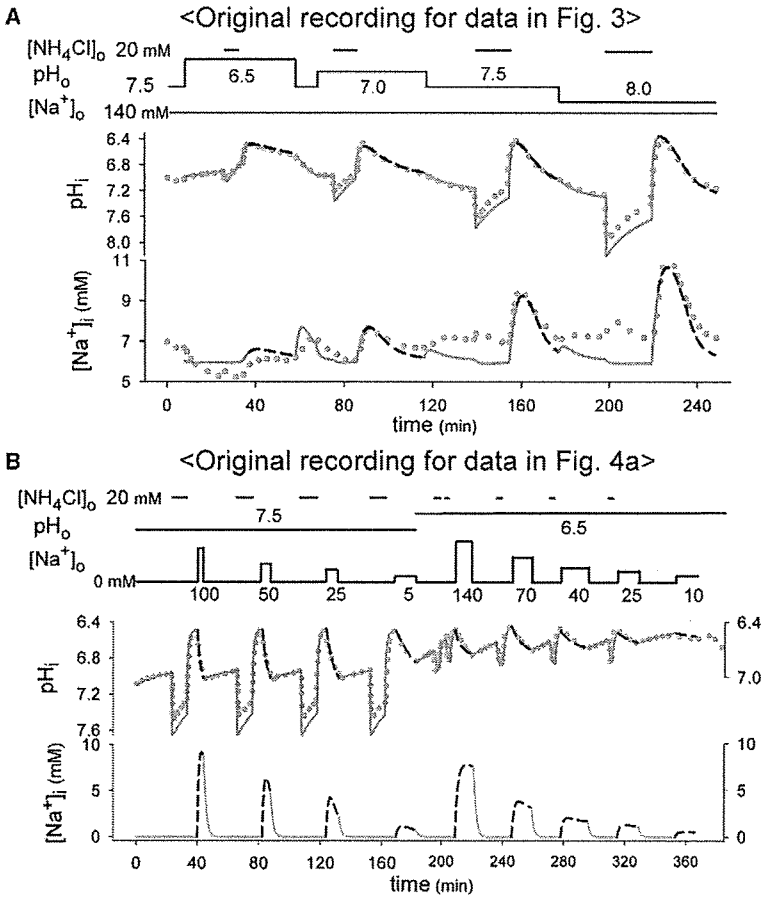

FIGURE 6 Simulations in various pH_o and $[Na^+]_o$. The experimental points (*shaded dots*) in panel *A* are from Fig. 6 in Vaughan-Jones and Wu (21) and those in panel *B* are from Fig. 1 in Wu and Vaughan-Jones (22). Dashed lines are simulated changes of pH_i and $[Na^+]_i$ in recovery periods from acidification. The values of model parameters were determined in a similar way to that in Fig. 5, except that N was already determined in the fitting procedure. In panel *B*, the parameters for J_{NaK} and $J_{p,Na+}$ determined in Fig. 5 were used, since $[Na^+]_i$ was not recorded in the original experiment. The values of model components are given in Table S3.

models had different numbers of unknown parameters. We found that the two models behaved differently in pH_o-induced inhibition (Fig. 3). *Mod2* could reconstruct the parallel shift of the pH_i-J_{NHE} relationship; that is, the activation foot moved to lower pH_i with decreasing pH_o (*arrows* in Fig. 3 *C*). Moreover, the pH_o-J_{NHE} relationship showed a clear saturation with increasing pH_o in agreement with experimental data (Fig. 3 *D*). In contrast, all the best-fit schemes of *Mod1* showed only scaling down in the NHE activity and failed to reconstruct the parallel shift of the pH_i-J_{NHE} and saturation by pH_o (Fig. 3, *A* and *B*). Therefore, we chose *Mod2* for characterizing the modulation by pH_o, which is in accord with the extracellular allosteric regulation suggested by Vaughan-Jones and Wu (21) and Vaughan-Jones and Spitzer (39).

Among the six plausible schemes for *Mod2*, we adopted the model using $n_H = 3$ with the eight-state ion-exchanging for the following simulations, simply because this model had the least χ^2, regardless of whether the difference between this and the other models was significant. The final parameter set (presented in Table S1) successfully reconstructed the dependencies on pH_i, $[Na^+]_o$, and $[Na^+]_i$ (Fig. 4, *A* and *B*), as well as the forward/reverse mode of NHE (Fig. 4, *C* and *D*) (15). We found that in the forward mode, the activation foot is determined by *Mod*, whereas the saturation at lower pH_i is dependent on j_{exch}. The slope is largely determined by cooperative activation in *Mod* with $n_H = 3$. In the reverse mode, j_{exch} and *Mod* change in opposite directions and J_{NHE} becomes bell-shaped.

Reconstruction of variations of pH_i and $[Na^+]_i$ in experimental recordings

Increase in $[Na^+]_i$ in NH_4Cl prepulse experiments

Wu and Vaughan-Jones (22) elaborated the experimental protocol shown in Fig. 5 *A* to examine effects of varying $[Na^+]_i$ on J_{NHE}. As the cell recovered from acidification in sections 6 and 8 in simulation (as depicted in Fig. 5), the counter Na^+ influx through NHE increased $[Na^+]_i$ to levels comparable to those in the experiment (Fig. 5 *B*). In both experiment and simulation, the range of $[Na^+]_i$ variation in section 6 was lower than that in section 8, and the initial rate of pH_i recovery was faster in section 6 (*inset* in Fig. 5). Since the simulation revealed that NH_3 and NH_4^+ were completely washed-out at $pH_i = 6.5$ (Fig. 5 *C*), it excluded the possibility that the remaining acid loading might retard recovery (an error factor mentioned in (21)). Thus, the

simulation results support the conclusion of Wu and Vaughan-Jones (22) that the different recovery speeds were caused by the depressed NHE activity at higher $[Na^+]_i$. For parameters of the cell model as well as mechanisms of inducing acidification by the NH_4Cl pulse, see Fig. 5 legend.

It is essential to consider variations of $[Na^+]_i$ as well as pH_i in evaluating the magnitude of J_{NHE}. We simulated the original recordings for obtaining the data points in Fig. 3 and Fig. 4 *A*, in which pH_o and $[Na^+]_o$ were varied. In the experiment (Fig. 6 *A*) giving the data points in Fig. 3, the recording protocol was analogous to section 8 in Fig. 5 and $[Na^+]_i$ varied over the range from 6 to 10 mM in both experiment and simulation. From the $[Na^+]_i$-J_{NHE} relationship (Fig. 4 *B*), it is evident that the magnitude of J_{NHE} in Fig. 3 is hardly affected by variations of $[Na^+]_i$ above 6 mM. On the other hand, the experimental protocol for the data points in Fig. 4 *A* (Fig. 6 *B*) is similar to that in section 6 in Fig. 5, and $[Na^+]_i$ increased from virtually 0 to various peak levels during recovery from acidification. Therefore, the amplitude of J_{NHE} in Fig. 4 *A* was clearly modified by the $[Na^+]_i$ variation, and that was why we supplemented individual experimental points in Fig. 4 *A* with corresponding values of $[Na^+]_i$ obtained by simulations (mentioned as preliminary simulations in Methods). Taken together, these simulation results confirmed that our NHE model is applicable when extracellular conditions are changed.

Acidification induced indirectly by blocking the Na^+/K^+ pump

An increase in $[Na^+]_i$ has been suggested to mediate the intracellular acidification when the Na^+/K^+ pump is inhibited through two mechanisms:

1. A depression of NHE activity due to a decrease in the transmembrane Na^+ gradient (40).
2. An induction of intracellular acidification linked to an increase of $[Ca^{2+}]_i$ through depression of Na^+-Ca^{2+} exchanger (NCX) (41,42).

First, we examined the extent of acidification induced by attenuating J_{NHE} through increased $[Na^+]_i$ (*black line* in Fig. 7). When 50% of the Na^+/K^+ pump was inhibited by 10 μM strophanthidin ($K_D = 1.12 \times 10^{-5}$ M (43)), $[Na^+]_i$ rose rapidly toward a saturating level beyond 16 mM, in agreement with the experimental data. However, pH_i was only reduced by 0.05, which was much smaller than the experimental drop of ~0.3. Next, we tested the second mechanism, in which an extra H^+ increment ($j_{inc,H+}$) occurs through an increase in $[Ca^{2+}]_i$ (*red line* in Fig. 7) (41). If $[Ca^{2+}]_i$ is mainly equilibrated by NCX in cardiac myocytes, $[Ca^{2+}]_i$ is a function of $[Na^+]_i^3$, provided that $[Ca^{2+}]_o$ and $[Na^+]_o$ remain constant:

$$\frac{[Ca^+]_i}{[Ca^+]_o} = \left(\frac{[Na^+]_i}{[Na^+]_o}\right)^3 \exp\left(\frac{V_m F}{RT}\right) \qquad (8)$$

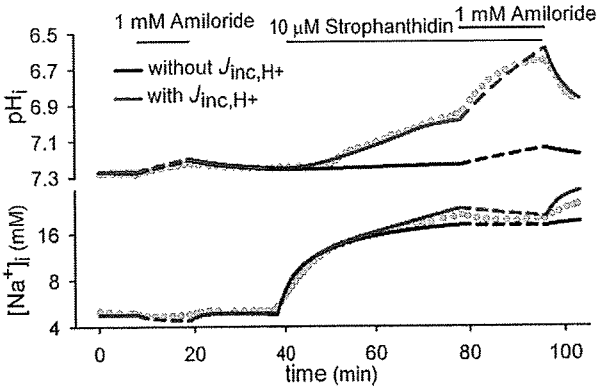

FIGURE 7 Effects of blocking the Na^+/K^+ pump on pH_i and $[Na^+]_i$. The original experimental recordings (*gray dots*) are taken from Fig. 2 in Kaila and Vaughan-Jones (42). Simulation results with (*red lines*) or without (*black lines*) an extra H^+ increment ($J_{inc,H+}$) are shown. Dashed lines indicate changes induced by applying amiloride. Most parameter values are the same as in Fig. 5, since the experimental conditions were comparable. The amplitudes of $J_{b,H+}$ and J_{NHE} were slightly modified to adjust the steady-state values of pH_i and $[Na^+]_i$ at time zero. The values of model components are given in Table S3.

(see Blaustein and Leder (44)). For simplicity, we assumed that $j_{inc,H+}$ is linearly proportional to $[Ca^{2+}]_i$ (or $[Na^+]_i^3$) within a limit (Eq. 18). In consequence, a decline of pH_i with an obvious delayed onset was obtained as in the experiment (see also (40)). In addition, the simulation successfully reconstructed the increased rate of acidification and the decrease of $[Na^+]_i$ during the complete blockage of NHE in the presence of strophanthidin in comparison to the control run. Although Eq. 18 is only a phenomenological description, the simulation supports the view that a Ca^{2+}-induced H^+ increment from an unknown origin contributes to acidification to a larger extent than depression of J_{NHE} through an increase in $[Na^+]_i$.

DISCUSSION

Here, for the first time to our knowledge, we have reconstructed the transient increase in $[Na^+]_i$ accompanying NHE activation at different $[Na^+]_o$ and pH_o. So far, there are two articles that offered simulated effects of acidosis on the developed tension with a cell model including electrical excitation, Ca^{2+} dynamics by the sarcoplasmic reticulum, contraction, and the modulation of various molecular functions at acidic pH_i (9,13). In contrast to those complicated simulations, we focused our simulations totally on the Purkinje fiber experiments, which recorded the time course of $[Na^+]_i$ variation caused by the NHE activation. For deeper understanding of regulation of $[Na^+]_i$ at different pH_i, we will discuss functional coupling between NHE and Na^+/K^+ pump during acidosis. We then determine the extent of $[Na^+]_i$ increase induced by acidosis using steady-state pH_i-$[Na^+]_i$ relationship, and discuss $[Na^+]_i$-J_{NHE} relationship by taking the thermodynamic driving force into account.

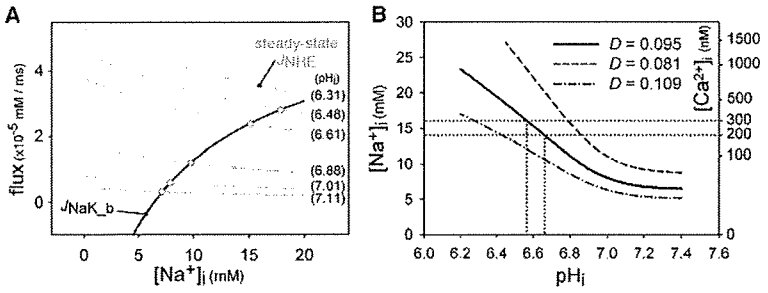

FIGURE 8 Steady-state relationship between pH_i and $[Na^+]_i$. (*A*) Na^+ flux balance between J_{NHE} and J_{NaK_b}. Gray curves indicate $[Na^+]_i$-J_{NHE} at the different pH_i values indicated on the right, and the black curve indicates J_{NaK_b}. Intersections of the J_{NHE} with J_{NaK_b} are marked with open circles. (*B*) The steady-state relationship between pH_i and $[Na^+]_i$, corresponding to intersections of the J_{NHE} and J_{NaK_b} in panel *A*. When the amplitude of the Na^+/K^+ pump was altered from $D = 0.095$ to $D = 0.081$ or 0.109, the curve shifted as indicated by the dashed lines. The steady-state $[Na^+]_i$ on the left axis was converted to $[Ca^{2+}]_i$ on the right axis using Eq. 8. The dotted lines indicate the critical levels of $[Na^+]_i$ and pH_i. The calculations were all conducted under the condition of a membrane potential of −52 mV, a reversal potential of K^+ at 20 mM $[K^+]_o$.

Relationship between acidosis and $[Na^+]_i$ or $[Ca^{2+}]_i$

The variation of $[Na^+]_i$ is determined by the balance among NHE, Na^+/K^+ pump, and passive Na^+ flux in our simple cell model. The time derivative of $[Na^+]_i$ is

$$\frac{d[Na^+]_i}{dt} = J_{NHE} - (J_{NaK} + J_{p,Na+})$$

(see Eq. 19). Since $[K^+]_o$ and the membrane potential are assumed to be constant, both J_{NaK} and $J_{p,Na+}$ are functions of only $[Na^+]_i$. To examine the major interaction between NHE and Na^+/K^+ pump, the sum of J_{NaK} and $J_{p,Na+}$ is treated as J_{NaK_b}, which is J_{NaK} biased by $J_{p,Na+}$ (Fig. 8 *A*). The intersections of the J_{NaK_b} and J_{NHE} curves correspond to $d[Na^+]_i/dt = 0$ and give steady-state values of $[Na^+]_i$ at each pH_i. This steady-state relationship is demonstrated by the continuous curve in Fig. 8 *B*. $[Na^+]_i$ is nearly constant on the alkaline side above pH_i 7.2 and increases linearly with acidosis. This Na^+ overload during persistent acidosis may affect cellular viability via a secondary $[Ca^{2+}]_i$ increment through NCX (45), which causes myocardial contracture. To investigate the critical level of acidosis, $[Na^+]_i$ is converted to $[Ca^{2+}]_i$ according to Eq. 8 (*right axis* in Fig. 8 *B*). Assuming that blood pumping of the ventricle is interfered with when diastolic $[Ca^{2+}]_i$ remains higher than the activation threshold of contraction at 200 or 300 nM, the critical $[Na^+]_i$ is 14–16 mM, or the critical pH_i is ~6.6. The critical pH_i moves in the acidic direction when J_{NaK} is depressed, and in the alkaline direction with enhanced J_{NaK} (*dotted lines* in Fig. 8 *B*). Similarly, the change in membrane leak conductance ($J_{p,Na+}$ in our model) under pathophysiological conditions may also affect the critical level of pH_i. To get a deeper insight into the critical level of acidosis, note that the pH sensitivity of channels, transporters, and contraction should also be accounted for in the model calculation in future.

Relationship between thermodynamic driving force and J_{NHE}

The variation of $[Na^+]_i$ affects the J_{NHE} via thermodynamic driving force, E_d, which is given as

$$E_d = RT \times \left(\ln\frac{[H^+]_i}{[H^+]_o} + \ln\frac{[Na^+]_o}{[Na^+]_i} \right). \quad (9)$$

With a constant pH_o/pH_i gradient and a fixed $[Na^+]_o$, E_d is a linear function of $\ln([Na^+]_i)$ and reverses its sign at an equilibrium value of $[Na^+]_i$ (Fig. 9 *A*). It should be noted that our model successfully defines the equilibrium value of $[Na^+]_i$ by adopting microscopic reversibility. Fig. 9 *A* indicates that the magnitude of J_{NHE} saturates below 3 mM $[Na^+]_i$ despite the linear increase of E_d. The dependency of J_{NHE} on E_d is given by the following equation, in analogy to Ohm's law,

$$J_{NHE} = gE_d, \quad (10)$$

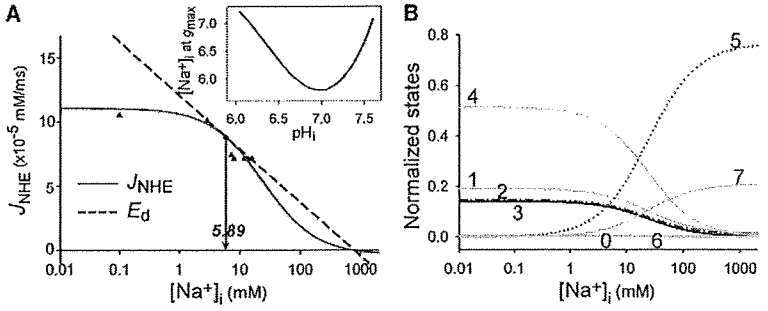

FIGURE 9 Variation of J_{NHE} and E_d, and transition of model states with $[Na^+]_i$. (*A*) The $[Na^+]_i$-J_{NHE} relationship (*solid line*) and E_d (*dashed line*) with a log scale for $[Na^+]_i$. J_{NHE} and data points (*triangles*) are identical, as shown in Fig. 4 *B*. E_d is zero at $[Na^+]_i = 787$ mM at $pH_i = 6.78$, $pH_o = 7.5$, and $[Na^+]_o = 150$ mM. (*Inset*) Point of tangency for g_{max} at each pH_i. (*B*) Distribution of states for the ion-exchanging part as a function of $[Na^+]_i$. Numerals indicate the states of NHE model, as defined in Fig. 1 *B*.

where g is the conductance of NHE (mol J^{-1} ms^{-1}) and is defined by the slope connecting each point on the J_{NHE} curve with the equilibrium point. The maximum g, g_{max}, appeared at $[Na^+]_i = 5.89$ mM, which is defined by a tangent line to the J_{NHE} at $pH_i = 6.78$. The values of $[Na^+]_i$ giving g_{max} were explored at various pH_i and are plotted against pH_i (*inset* of Fig. 9). It is evident that $[Na^+]_i$ at g_{max} remains in a narrow range over a wide range of pH_i; that is, the NHE model operates almost at g_{max} over the physiological range of $[Na^+]_i$, even during severe acidosis.

The $[Na^+]_i$ dependency of J_{NHE} or g is determined by the state distributions of the ion-exchanging part of the NHE model, as shown in Fig. 9 *B*:

$$J_{NHE} \propto (\text{state } 2)k_1^+ - (\text{state } 5)k_1^-. \tag{11}$$

When intracellular Na^+ is depleted, state 5, in which Na^+ binds on the intracellular side, becomes nearly 0. Accordingly, J_{NHE} is only dependent on state 2, thereby causing J_{NHE} to saturate. As $[Na^+]_i$ increases, states 5 and 7 accumulate at the expense of all the other states. An integrated effect of the variations of states 2 and 5 induces a gradual decay of g with increasing $[Na^+]_i$. Thus, the state rearrangement produces the sigmoidal dependency of J_{NHE} on $[Na^+]_i$ (Fig. 9 *A*).

APPENDIX

Equations for the simple cell model

$$CF_X = \frac{z_X F V_m}{RT} \frac{[X]_i - [X]_o \exp(-z_X F V_m/RT)}{1 - \exp(-z_X F V_m/RT)}, \text{ where}$$
$$X = \{Na^+, NH_4^+\}. \tag{12}$$

$$J_{p,Na+} = P_{Na+} CF_{Na+}. \tag{13}$$

$$J_{b,H+} = A[H^+]_o + B\,pH_i + C. \tag{14}$$

$$J_{NaK} = D \frac{3 \times I_{NaK(\text{in kyoto model})}}{F\,vol_i}. \tag{15}$$

$$J_{NH4+} = P_{NH4+} CF_{NH4+}. \tag{16}$$

$$J_{NH3} = P_{NH3}([NH_3]_i - [NH_3]_o). \tag{17}$$

$$J_{inc,H+} = \begin{cases} E([Na^+]_i)^3 & (\text{when } J_{inc,H+} < Max_{inc,H+}) \\ Max_{inc,H+} & (\text{otherwise}) \end{cases}. \tag{18}$$

$$\frac{d[Na^+]_i}{dt} = J_{NHE} - J_{NaK} - J_{p,Na+}. \tag{19}$$

$$\frac{d([NH_3]_i + [NH_4^+]_i)}{dt} = -J_{NH3} - J_{NH4+}. \tag{20}$$

$$\frac{d([H^+]_i + [NH_4^+]_i + [HA]_i + [HB]_i)}{dt} = -J_{NHE} - J_{b,H+} - J_{NH4+} + J_{inc,H+}. \tag{21}$$

The following equilibrium reactions among NH_3, NH_4^+, H^+, and pH buffer A and B were calculated.

$$HA \overset{K_A}{\rightleftharpoons} A^- + H^+.$$

$$HB \overset{K_B}{\rightleftharpoons} B^- + H^+.$$

$$NH_4^+ \overset{K_{NH3}}{\rightleftharpoons} NH_3 + H^+.$$

$$[HA]_i + [A^-]_i = [TA]. \tag{22}$$

$$[HB]_i + [B^-]_i = [TB]. \tag{23}$$

$$K_A = \frac{[A^-]_i [H^+]_i}{[HA]_i}. \tag{24}$$

$$K_B = \frac{[B^-]_i [H^+]_i}{[HB]_i}. \tag{25}$$

$$K_{NH3} = \frac{[NH_3]_i [H^+]_i}{[NH_4^+]_i} = \frac{[NH_3]_o [H^+]_o}{[NH_4^+]_o}. \tag{26}$$

[TA] or [TB] is the total concentration of pH buffer of A or B, respectively. $[NH_3]_i$, $[NH_4^+]_i$, and $[H^+]_i$ were obtained by solving Eqs. 22–26 with the iteration method.

Definitions and values of the model parameters are given in Table S3.

SUPPORTING MATERIAL

One figure and three tables are available at http://www.biophysj.org/biophysj/supplemental/S0006-3495(09)01444-1.

The authors are grateful to Prof. T. Powell and colleagues in the Biosimulation projects of Kyoto University and Ritsumeikan University for continuous discussion during this study.

This work was supported by the Biomedical Cluster Kansai project of Ministry of Education, Culture, Sports, Science and Technology Japan.

REFERENCES

1. Leem, C. H., D. Lagadic-Gossmann, and R. D. Vaughan-Jones. 1999. Characterization of intracellular pH regulation in the guinea-pig ventricular myocyte. *J. Physiol.* 517:159–180.
2. Yamamoto, T., P. Swietach, A. Rossini, S. H. Loh, R. D. Vaughan-Jones, et al. 2005. Functional diversity of electrogenic Na^+-HCO_3^- cotransport in ventricular myocytes from rat, rabbit and guinea pig. *J. Physiol.* 562:455–475.
3. Vaughan-Jones, R. D., F. C. Villafuerte, P. Swietach, T. Yamamoto, A. Rossini, et al. 2006. pH-Regulated Na^+ influx into the mammalian ventricular myocyte: the relative role of Na^+-H^+ exchange and Na^+-HCO co-transport. *J. Cardiovasc. Electrophysiol.* 17 (Suppl 1):S134–S140.

4. ten Hove, M., J. G. van Emous, and C. J. van Echteld. 2003. Na^+ overload during ischemia and reperfusion in rat hearts: comparison of the Na^+/H^+ exchange blockers EIPA, cariporide and eniporide. *Mol. Cell. Biochem.* 250:47–54.
5. Hartmann, M., and U. K. Decking. 1999. Blocking Na^+-H^+ exchange by cariporide reduces Na^+-overload in ischemia and is cardioprotective. *J. Mol. Cell. Cardiol.* 31:1985–1995.
6. Kentish, J. C. 1999. A role for the sarcolemmal Na^+/H^+ exchanger in the slow force response to myocardial stretch. *Circ. Res.* 85:658–660.
7. Cingolani, H. E., N. G. Perez, E. A. Aiello, and M. C. de Hurtado. 2005. Intracellular signaling following myocardial stretch: an autocrine/paracrine loop. *Regul. Pept.* 128:211–220.
8. Crampin, E. J., N. P. Smith, A. E. Langham, R. H. Clayton, and C. H. Orchard. 2006. Acidosis in models of cardiac ventricular myocytes. *Philos. Transact. A Math. Phys. Eng. Sci.* 364:1171–1186.
9. Ch'en, F. F., R. D. Vaughan-Jones, K. Clarke, and D. Noble. 1998. Modeling myocardial ischemia and reperfusion. *Prog. Biophys. Mol. Biol.* 69:515–538.
10. Swietach, P., and R. D. Vaughan-Jones. 2005. Spatial regulation of intracellular pH in the ventricular myocyte. *Ann. N.Y. Acad. Sci.* 1047:271–282.
11. Alexander, R. T., A. Malevanets, A. M. Durkan, H. S. Kocinsky, P. S. Aronson, et al. 2007. Membrane curvature alters the activation kinetics of the epithelial Na^+/H^+ exchanger, NHE3. *J. Biol. Chem.* 282:7376–7384.
12. Weinstein, A. M. 1995. A kinetically defined Na^+/H^+ antiporter within a mathematical model of the rat proximal tubule. *J. Gen. Physiol.* 105:617–641.
13. Crampin, E. J., and N. P. Smith. 2006. A dynamic model of excitation-contraction coupling during acidosis in cardiac ventricular myocytes. *Biophys. J.* 90:3074–3090.
14. Niederer, S. A., and N. P. Smith. 2007. A mathematical model of the slow force response to stretch in rat ventricular myocytes. *Biophys. J.* 92:4030–4044.
15. Wakabayashi, S., T. Hisamitsu, T. Pang, and M. Shigekawa. 2003. Kinetic dissection of two distinct proton binding sites in Na^+/H^+ exchangers by measurement of reverse mode reaction. *J. Biol. Chem.* 278:43580–43585.
16. Moncoq, K., G. Kemp, X. Li, L. Fliegel, and H. S. Young. 2008. Dimeric structure of human Na^+/H^+ exchanger isoform 1 overproduced in *Saccharomyces cerevisiae*. *J. Biol. Chem.* 283:4145–4154.
17. Otsu, K., J. Kinsella, B. Sacktor, and J. P. Froehlich. 1989. Transient state kinetic evidence for an oligomer in the mechanism of Na^+-H^+ exchange. *Proc. Natl. Acad. Sci. USA.* 86:4818–4822.
18. Otsu, K., J. L. Kinsella, P. Heller, and J. P. Froehlich. 1993. Sodium dependence of the Na^+-H^+ exchanger in the pre-steady state. Implications for the exchange mechanism. *J. Biol. Chem.* 268:3184–3193.
19. Lacroix, J., M. Poet, C. Maehrel, and L. Counillon. 2004. A mechanism for the activation of the Na/H exchanger NHE-1 by cytoplasmic acidification and mitogens. *EMBO Rep.* 5:91–96.
20. Fuster, D., O. W. Moe, and D. W. Hilgemann. 2008. Steady-state function of the ubiquitous mammalian Na/H exchanger (NHE1) in relation to dimer coupling models with 2Na/2H stoichiometry. *J. Gen. Physiol.* 132:465–480.
21. Vaughan-Jones, R. D., and M. L. Wu. 1990. Extracellular H^+ inactivation of Na^+-H^+ exchange in the sheep cardiac Purkinje fiber. *J. Physiol.* 428:441–466.
22. Wu, M. L., and R. D. Vaughan-Jones. 1997. Interaction between Na^+ and H^+ ions on Na-H exchange in sheep cardiac Purkinje fibers. *J. Mol. Cell. Cardiol.* 29:1131–1140.
23. Aronson, P. S. 1985. Kinetic properties of the plasma membrane Na^+-H^+ exchanger. *Annu. Rev. Physiol.* 47:545–560.
24. Green, J., D. T. Yamaguchi, C. R. Kleeman, and S. Muallem. 1988. Cytosolic pH regulation in osteoblasts. Interaction of Na^+ and H^+ with the extracellular and intracellular faces of the Na^+/H^+ exchanger. *J. Gen. Physiol.* 92:239–261.
25. Wallert, M. A., and O. Frohlich. 1989. Na^+-H^+ exchange in isolated myocytes from adult rat heart. *Am. J. Physiol.* 257:C207–C213.
26. van Borren, M. M., A. Baartscheer, R. Wilders, and J. H. Ravesloot. 2004. NHE-1 and NBC during pseudo-ischemia/reperfusion in rabbit ventricular myocytes. *J. Mol. Cell. Cardiol.* 37:567–577.
27. Jean, T., C. Frelin, P. Vigne, P. Barbry, and M. Lazdunski. 1985. Biochemical properties of the Na^+/H^+ exchange system in rat brain synaptosomes. Interdependence of internal and external pH control of the exchange activity. *J. Biol. Chem.* 260:9678–9684.
28. Bountra, C., T. Powell, and R. D. Vaughan-Jones. 1990. Comparison of intracellular pH transients in single ventricular myocytes and isolated ventricular muscle of guinea-pig. *J. Physiol.* 424:343–365.
29. Petrecca, K., R. Atanasiu, S. Grinstein, J. Orlowski, and A. Shrier. 1999. Subcellular localization of the Na^+/H^+ exchanger NHE1 in rat myocardium. *Am. J. Physiol.* 276:H709–H717.
30. Hoffmann, G., Y. Ko, A. Sachinidis, B. O. Gobel, H. Vetter, et al. 1995. Kinetics of Na^+/H^+ exchange in vascular smooth muscle cells from WKY and SHR: effects of phorbol ester. *Am. J. Physiol.* 268:C14–C20.
31. Ng, L. L., J. E. Davies, M. Siczkowski, F. P. Sweeney, P. A. Quinn, et al. 1994. Abnormal Na^+/H^+ antiporter phenotype and turnover of immortalized lymphoblasts from type 1 diabetic patients with nephropathy. *J. Clin. Invest.* 93:2750–2757.
32. Siczkowski, M., J. E. Davies, and L. L. Ng. 1994. Activity and density of the Na^+/H^+ antiporter in normal and transformed human lymphocytes and fibroblasts. *Am. J. Physiol.* 267:C745–C752.
33. Vaughan-Jones, R. D., and M. L. Wu. 1990. pH dependence of intrinsic H^+ buffering power in the sheep cardiac Purkinje fiber. *J. Physiol.* 425:429–448.
34. Sun, B., C. H. Leem, and R. D. Vaughan-Jones. 1996. Novel chloride-dependent acid loader in the guinea-pig ventricular myocyte: part of a dual acid-loading mechanism. *J. Physiol.* 495:65–82.
35. Niederer, S. A., P. Swietach, D. A. Wilson, N. P. Smith, and R. D. Vaughan-Jones. 2008. Measuring and modeling chloride-hydroxyl exchange in the Guinea-pig ventricular myocyte. *Biophys. J.* 94:2385–2403.
36. Matsuoka, S., N. Sarai, S. Kuratomi, K. Ono, and A. Noma. 2003. Role of individual ionic current systems in ventricular cells hypothesized by a model study. *Jpn. J. Physiol.* 53:105–123.
37. Mitra, R. L., and M. Morad. 1991. Permeance of Cs^+ and Rb^+ through the inwardly rectifying K^+ channel in guinea pig ventricular myocytes. *J. Membr. Biol.* 122:33–42.
38. Bielen, F. V., H. G. Glitsch, and F. Verdonck. 1991. Dependence of Na^+ pump current on external monovalent cations and membrane potential in rabbit cardiac Purkinje cells. *J. Physiol.* 442:169–189.
39. Vaughan-Jones, R. D., and K. W. Spitzer. 2002. Role of bicarbonate in the regulation of intracellular pH in the mammalian ventricular myocyte. *Biochem. Cell Biol.* 80:579–596.
40. Deitmer, J. W., and D. Ellis. 1980. Interactions between the regulation of the intracellular pH and sodium activity of sheep cardiac Purkinje fibers. *J. Physiol.* 304:471–488.
41. Vaughan-Jones, R. D., W. J. Lederer, and D. A. Eisner. 1983. Ca^{2+} ions can affect intracellular pH in mammalian cardiac muscle. *Nature.* 301:522–524.
42. Kaila, K., and R. D. Vaughan-Jones. 1987. Influence of sodium-hydrogen exchange on intracellular pH, sodium and tension in sheep cardiac Purkinje fibers. *J. Physiol.* 390:93–118.
43. Levi, A. J. 1991. The effect of strophanthidin on action potential, calcium current and contraction in isolated guinea-pig ventricular myocytes. *J. Physiol.* 443:1–23.
44. Blaustein, M. P., and W. J. Lederer. 1999. Sodium/calcium exchange: its physiological implications. *Physiol. Rev.* 79:763–854.
45. Baartscheer, A. 2006. Chronic inhibition of Na^+/H^+-exchanger in the heart. *Curr. Vasc. Pharmacol.* 4:23–29.
46. Boron, W. F., and P. De Weer. 1976. Intracellular pH transients in squid giant axons caused by CO_2, NH_3, and metabolic inhibitors. *J. Gen. Physiol.* 67:91–112.
47. Benjelloun, F., N. Bakouh, J. Fritsch, P. Hulin, J. Lipecka, et al. 2005. Expression of the human erythroid Rh glycoprotein (RhAG) enhances both NH_3 and NH_4^+ transport in HeLa cells. *Pflugers Arch.* 450:155–167.

FEBS Letters 583 (2009) 3600–3604

ELSEVIER

FEBS Letters

journal homepage: www.FEBSLetters.org

Essential role of TRPV2 ion channel in the sensitivity of dystrophic muscle to eccentric contractions

Nadège Zanou [a], Yuko Iwata [b], Olivier Schakman [a], Jean Lebacq [a], Shigeo Wakabayashi [b], Philippe Gailly [a,*]

[a] Laboratory of Cell Physiology, Institute of Neurosciences, Université catholique de Louvain, 55/40 av. Hippocrate, 1200 Brussels, Belgium
[b] Department of Molecular Physiology, National Cardiovascular Center Research Institute Suita, Osaka 565-8565, Japan

ARTICLE INFO

Article history:
Received 4 September 2009
Revised 9 October 2009
Accepted 12 October 2009
Available online 17 October 2009

Edited by Gianni Cesareni

Keywords:
Eccentric contraction
Calcium
TRPV2
Duchenne muscular dystrophy

ABSTRACT

Duchenne myopathy is a lethal disease due to the absence of dystrophin, a cytoskeletal protein. Muscles from dystrophin-deficient mice (*mdx*) typically present an exaggerated susceptibility to eccentric work characterized by an important force drop and an increased membrane permeability consecutive to repeated lengthening contractions. The present study shows that mdx muscles are largely protected from eccentric work-induced damage by overexpressing a dominant negative mutant of TRPV2 ion channel. This observation points out the role of TRPV2 channel in the physiopathology of Duchenne muscular dystrophy.

1. Introduction

Duchenne muscular dystrophy (DMD) is a progressive neuromuscular disease affecting 1/3500 male birth (reviewed in [1,2]). It is characterized by an important muscle degeneration (foci of necrotic fibers) followed, at early stages, by an intense regeneration process. As the regenerative capacity diminishes, muscle tissue is progressively replaced by adipose and fibrous connective tissue, leading to an important muscle weakness. This pathology results from a mutation in the Xp21 locus, which leads to the lack of expression of dystrophin, a 427 kDa protein located at the cytoplasmic face of the sarcolemma [3,4]. In normal skeletal muscle cells, dystrophin is associated, at its carboxy-terminal domain, with a complex of transmembrane proteins constituted of β-dystroglycan and α-, β-, γ- and δ-sarcoglycans and called the dystrophin–glycoprotein complex (DGC [5,6]). The complex also binds to merosin (laminin-2), a component of the extracellular matrix. At its amino-terminal domain, dystrophin binds to cytoskeletal F-actin filaments (i.e. non-sarcomeric actin). Dystrophin thus constitutes a link between the cytoskeleton and the extracellular matrix [7]. The alteration of dystrophin expression has two main consequences: (i) it affects DGC targeting to the membrane and therefore causes a disruption of the link between the cytoskeleton and the extracellular matrix that could induce membrane fragility; (ii) it induces a disorganization of the cytoskeleton and leads to a disregulation of several ion channel types such as the acetylcholine receptor [8] and stretch-activated and stretch-inactivated channels [9–11]. The mechanism by which the absence of dystrophin leads to muscle fiber death remains partially unknown, but an abnormal entry of Ca^{2+} through membrane tears caused by the absence of dystrophin or through abnormally regulated channels seems to play a major role (reviewed in [12,13]). Indeed, in muscles from *mdx* mice, a genetic model of Duchenne muscular dystrophy, this abnormal entry of Ca^{2+} has been proved to activate several signaling cascades involved in cell damage such as Ca^{2+}-activated proteases (calpains) [14–16], phospholipase A_2 [17,18], accumulation of Ca^{2+} in the mitochondria [19] and production of ROS [20,21].

Recently, the involvement of a specific ion channel called TRPV2 in the pathophysiology of DMD was proposed [22]. TRPV2 protein belongs to the large family of TRP cationic channels involved in various processes of sensory signaling (sensing heat and cold, pH, osmolarity, etc. for review, see [23]). TRPV2 is activated by membrane stretch [24]. It normally localizes in the intracellular membrane compartments but translocates to the plasma membrane in dystrophic muscle fibers [25]. Its specific inhibition was shown to ameliorate muscular dystrophy. Indeed, *mdx* mice expressing a dominant negative mutant TRPV2 channel presented a reduced entry of Ca^{2+} in muscle fibers; as a consequence, they exhibited reduced muscle degeneration (necrosis and apoptosis) and regeneration (central nuclei, etc.). These observations suggest that TRPV2 channel constitutes the principal Ca^{2+} entry pathway in dystrophic muscle fibers.

* Corresponding author. Fax: +32 2 7645580.
E-mail address: philippe.gailly@uclouvain.be (P. Gailly).

0014-5793/$36.00 © 2009 Federation of European Biochemical Societies. Published by Elsevier B.V. All rights reserved.
doi:10.1016/j.febslet.2009.10.033